Energy Conversion and Management 229 (2021) 113734

Contents lists available at ScienceDirect

Energy Conversion and Management

journal homepage: www.elsevier.com/locate/enconman

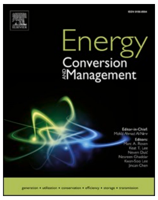

Validation of robustness and fuel efficiency of a universal model-based energy management strategy for fuel cell hybrid trains: From analytical derivation via simulation to measurement on test bench☆

Hujun Peng [a,*], Hanqing Cao [a], Steffen Dirkes [b], Zhu Chen [a], Kai Deng [a], Jonas Gottschalk [b], Cem Ünlübayir [c], Andreas Thul [a], Lars Löwenstein [d], Dirk Uwe Sauer [c], Stefan Pischinger [b], Kay Hameyer [a]

[a] *Institute of Electrical Machines (IEM), RWTH Aachen University, Aachen, Germany*
[b] *Institute for Combustion Engines (VKA), RWTH Aachen University, Aachen, Germany*
[c] *Chair for Electrochemical Energy Conversion and Storage Systems, Institute for Power Electronics and Electrical Drives (ISEA), RWTH Aachen University, Aachen, Germany*
[d] *Siemens Mobility GmbH, Vienna, Austria*

ARTICLE INFO

Keywords:
Fuel cell trains
APMP
Universality
Robustness
Experimental validation

ABSTRACT

Fuel cell hybrid trains are being commercialized to replace trains powered by combustion engine to reduce carbon dioxide emission without high investment cost in overhead catenaries. In this context, this paper presents a universal model-based strategy for the operation of fuel cell hybrid trains based on adaptive Pontryagin's minimum principle (APMP). Different from all other work, the implementation of Pontryagin's minimum principle (PMP) considers the relaxation process due to the resistance-capacitor branches in the batteries to provide a precise reference for the evaluation of the robustness and fuel economy of the APMP-based strategy. Furthermore, a formula to physically estimate the costate is inspired by the offline PMP results and derived by using the energy conservation principle. Moreover, the robustness of the strategy against fuel cell aging, battery aging, inaccurate fuel cell modeling, and deviations introduced through fitting experimental data is investigated through simulation. Compared to the offline results, a maximum 1.5% higher hydrogen consumption is observed by simulation under different aging and uncertain operating conditions. Finally, the effectiveness and the robustness of the strategy are validated through measurement on the test bench at the Center for Mobile Propulsion of the RWTH Aachen University. A maximum of 2.7% more hydrogen consumption is measured compared to the offline PMP results under various conditions of uncertainty.

1. Introduction

1.1. Background

In July 2020, European Commission has released its hydrogen strategy for a climate-neutral Europe and a roadmap to 2050 is also provided. The primary goal is to produce clean hydrogen with renewable electricity and to boost hydrogen consumption of end-users. From 2020 up to 2024, at least six GW hydrogen electrolyzers will be installed in the EU. In the second phase, from 2025 to 2030, more than 40 GW hydrogen electrolyzers will be installed. In the third phase, from 2030 towards 2050, electricity from hydrogen should be used in all hard-to-decarbonize sectors [1]. Besides hydrogen production, the demand for hydrogen will be boosted in end-user sectors, including industry application and mobility. In transport, hydrogen-powered vehicles are promising alternatives to combustion engine-driven ones, and more public transport vehicles powered by hydrogen have already entered the market. Notably, the world's first commercial hydrogen-powered train named *Coradia iLint* began its service in Germany, 2018, and a total of 41 trains have been ordered. The Netherlands will be the second country to

---

☆ This work is funded by the German Federal Ministry of Transport and Digital Infrastructure (BMVi) under the National Innovation Program Hydrogen and Fuel Cell Technology (NIP) with the funding numbers of 03B10502B and 03B10502B2. The authors gratefully acknowledge the support by Siemens AG, Ballard, and NIP.

* Corresponding author.
E-mail address: hujun.peng@iem.rwth-aachen.de (H. Peng).

https://doi.org/10.1016/j.enconman.2020.113734
Received 29 August 2020; Received in revised form 21 November 2020; Accepted 1 December 2020

prove the emission-free solution for no-electrified lines [2]. Siemens is also working with RWTH Aachen University to develop a high-power-fuel-cell-hybrid-train, with fuel cell systems provided by Ballard Power Systems, which is the background of this contribution [3].

1.2. Literature review

For hydrogen-power trains, besides the fuel cell system, a high-power-density lithium battery system is used to assist traction and recycle energy during regenerative braking. Due to the hybrid configuration of power sources, the power distribution between them, named energy management, can be used to improve the performance of the hybrid trains. The main goal is to minimize hydrogen consumption under different driving conditions, while reducing the component degradation at the same time. Furthermore, the hybrid train operates under charge-sustaining conditions instead of a plug-in operation. Therefore, the State of Charge (SoC) of the battery should be maintained within the required range to avoid overcharging and over-discharging of battery cells. There are a lot of research articles in the field of energy management strategies for fuel cell hybrid vehicles, and they can be categorized into three types, including rule-based, optimization-based, and learning-based methods. The rule-based approach uses heuristic experiences and is implemented as deterministic or fuzzy logic-based rules whose computational load is low. In [4], a rule-based strategy implemented by a finite state machine is introduced with robustness against different driving conditions. However, the rules are extracted purely heuristically, and it is not straightforward to prove the correctness of the choice of parameters. In [5,6], the fuzzy logic-based strategies are used, whereby the parameters of the membership function are optimized by using genetic algorithms with a previously defined cost function to be minimized. Even though the fuzzy logic control is famous for its robustness, it is not convincing that this strategy performs well under various and unpredictable driving conditions, because the parameters are optimized only for training driving cycles. For the learning-based method, no model or experiences are needed, and the algorithm is based on training data resulted from offline strategies [7]. However, the learning-based method requires large amounts of data, which limits its adaptivity if the driving condition is not trained before. Furthermore, the effectiveness of reinforcement learning is rather sensitive to parameter selections [8]. For the optimization-based method, there are two subtypes, including global optimization-based and local optimization-based methods. The global optimization-based method includes dynamic programming and Pontryagin's minimum principle (PMP)-based method. In [9,10], these global optimization-based methods are introduced. However, they can not be implemented in real-time because information about the entire driving cycle is required as prior knowledge. Therefore, the results from the offline strategy can be used as a benchmark to evaluate other real-time strategies and to exact rules for the rule-based strategy [11]. For the local optimization-based method, equivalent consumption minimization strategy (ECMS) and adaptive Pontryagin's minimum principle (APMP) are primarily found in the literature. The ECMS can be derived from APMP mathematically; Therefore, they are essentially the same. For them, the largest challenge lies in the adaptive update of the costate or the equivalent factor according to driving conditions without loss of causality. In some literature, a PI-controller is used to adjust the factors according to the SoC values. However, the set up of the controller parameters is also challenging. In [12], a multi-mode equivalent energy consumption method is used to distribute power between fuel cells, batteries, and capacitors. Thereby, during different driving phases, such as parking, traction, coasting, or braking, the power requirement for fuel cell is set to maximize the working efficiency during respective periods. However, various parameters, which are not physically derived, are introduced into the strategy, limiting the transferability to other conditions. Moreover, maximizing efficiency in each driving phase does not lead to maximal efficiency along the whole driving cycle. If component aging occurs, the robustness of this strategy remains troublesome because many of the parameters mentioned above depend on component characteristics. In [13,14], driving pattern recognition is used to update the equivalent factor, and Markov-based velocity prediction is implemented to predict the future driving condition. However, the candidates of the equivalent factors are limited to training samples, which, therefore, limits its robustness and adaptivity. In a few articles, such as [15,16], the range of the costate is physically derived, which is not dependent on specific driving cycles. However, within the bounds, the costate is assumed to be a linear or quadratic function of SoC, which is not physically proven. Moreover, the amplitude of the costate decreases as SoC increases, which is not correct, because the open-circuit voltage of batteries increases as SoC increases, and so should the magnitude of the costate [10]. Besides good fuel economy under the deterministic framework, the strategy should be robust against uncertainties. In [17], various uncertainties, including the ones in hybrid energy sources, auxiliary services, driving subsystems, and load condition, are introduced. For that, a sub-optimal real-time strategy with these uncertainties considered is implemented. This strategy uses the ECMS as the primary strategy and fuzzy logic control to compensate for the fuel cell power as the aging of components increased. However, the parameters of the membership function remain crucial, as mentioned above. Furthermore, components suffer from the aging process. Compared to batteries, the fuel cell system is much more sensitive to operation conditions, like water management and load dynamic, which makes the robustness of strategies against component uncertainties necessary [18]. In [4], a simple formula to predict the performance degradation of fuel cells dependent on transient power load, start/stop, idling, and high power load is validated through the experiment. The degradation model is integrated into the energy management to reduce cost over the entire lifespan of vehicles. In [19], an adaptive ECMS is used to distribute power between fuel cells, batteries, and capacitors. Thereby, the equivalent factor is adjusted according to the aged models of fuel cells and battery. However, the equivalent factor is adjusted by using heuristic mathematical formulas to realize charge sustaining conditions as closely as possible, which is not generalized enough and can not ensure its robustness under different driving conditions.

Summarily, ECMS, or APMP is a promising method to minimize hydrogen consumption in real-time applications. However, the estimating of the costate is based on heuristic formulas or trained under various training samples. In this way, the effectiveness of the strategy is limited. The practical applications are especially troublesome due to numerous uncertainties and component aging. The robustness of the energy management becomes cumbersome due to the lack of model-based formula to estimate the costate or the equivalent factor, even though the literature recognizes the energy management robustness as particularly advantageous property. In order to solve this problem, [10] introduces a model-based method to correct the costate. Thereby, a formula is inspired by the offline PMP results and derived by using the optimal control theory in a reverse way. However, dynamics in the parallel resistance-capacitor branches of the battery system are not considered in obtaining the costate, which will be solved in this contribution.

1.3. Main work

The most significant contribution of this work is to design and validate a scalable, robust APMP-based strategy for fuel cell hybrid vehicles. The costate is regularly corrected by using an analytical formula, which is derived based on the energy conservation principle. Different from all other research contributions, the offline PMP considers more accurate battery models, with various resistance-capacitor branches included, which provides a precise reference to evaluate the online APMP strategy regarding fuel economy and robustness. Moreover, the robustness of the APMP-based approach against fuel cell aging, battery aging, inconsistency between modeling used in energy management and the actual system, as well as deviations introduced through fitting experiment data, are proved by using simulation and experimental measurement. Because of its model-based characteristic, it is easy to be transferred to other transportation or stationary applications.

1.4. Paper organization

This work is organized as follows: In Section 2, the configuration of the hybrid driveline is briefly introduced. Thereby, the influence of various operation conditions on the specific consumption curve or the efficiency curve of the fuel cell system is introduced. In Section 3, the offline PMP algorithm considering relaxation processes in batteries is firstly introduced. Then, the formula to estimate the costate is derived based on the energy conservation principle. After that, the algorithm of APMP is presented. In Section 4, the effectiveness and the robustness of the APMP-based strategy against various uncertainties in fuel cell and battery modeling, as well as aging effects, are proved based on simulation results. In Section 5, the configuration of the test bench is presented, and the robustness of the APMP-based method is verified through measurement. In Section 6, the conclusions will be given.

2. Driveline

In the following sections, the driveline configuration, the battery system, and fuel cell system will be explained in detail, and a respective overview of the modeling of other components of the drive line can be found in [11].

2.1. Dirveline configuration

This section provides a brief overview of the hybrid train. The configuration, which is utilized in the simulations in subsequent chapters, is displayed in Fig. 1.

This hybrid train is powered by two sources, a fuel cell system and a lithium-ion battery system. As the primary energy source, the fuel cell system is actively controlled by a unidirectional DC/DC converter. The lithium-ion battery system is directly connected to the DC bus of the fuel cell output to assist acceleration and store back the energy during regenerative braking. For this purpose, a bidirectional DC/DC boost converter is utilized as an interface from fuel cell output to the DC-link. Auxiliary equipment, which is modeled as constant power load, is all attached to DC-link, and includes heating, compressors, ventilation systems, and air conditioning system. The power rating of auxiliary units is assumed to be 39 kW in summer and 67.7 kW in winter. After the DC-link, the electric power is fed to electric motors through an inverter, and then finally converted to mechanical power by the electric motors. In addition, the electric motor can also operate as a generator to recuperate the mechanical energy from braking. The mechanical torque from the electric motor shaft is transmitted to the axle and tires of the train through the gear system.

Regarding the environment conditions, four different driving cycles and corresponding terrain profiles of three different routes are defined, as shown in Fig. 2. The distances and travel time corresponding to all four driving cycles are listed in Table 1. Moreover, the number of passengers is assumed to be 120 regarding all four driving cycles, with an average passenger weight of 75 kg.

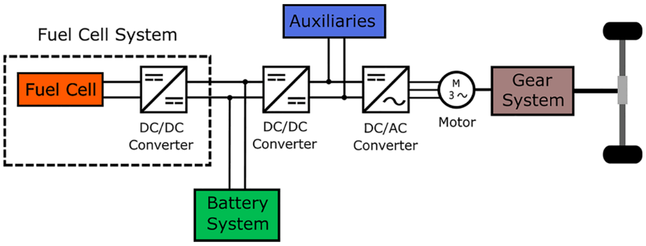

Fig. 1. System configuration of the hybrid train.

2.2. Fuel cell system

Two Proton-exchange membranes (PEM) fuel cell systems supplied by the company Ballard Power Systems are used in the experiment, including *HD7* and *HD8*. Thereby, the maximal power of *HD7* is 100 kW, while *HD8* can output 200 kW net power. Their specific consumption curves can be found in Fig. 3a. Furthermore, the fuel cell system's efficiency curve depends strongly on the operational conditions [18]. In Fig. 3b and c, the influence of the coolant temperature at stack inlet and the differential pressure across the membrane on the system efficiency of *HD7* is displayed, respectively. Moreover, the fuel cell system suffers from the aging process with time, and the influence of fuel cell degradation on *HD7*'s system efficiency is displayed in Fig. 3d, whereby the efficiency decreases with aging. Since the fuel cell system's characteristic curves suffer from some degree of uncertainty of both short-term and long-term, the energy management strategy should show robustness to maintain a high fuel economy even though the performance of the fuel cell system varies.

2.3. Battery system

The high-performance lithium-ion cell used in this work is modeled through a third-order equivalent electrical circuit and parameterized by the measurement data. Regarding the high-power requirement from the train, battery pack with technical specifications listed in Table 2 is utilized. The dependency of the battery open-circuit voltage and the internal resistance on the battery SoC is shown in Fig. 5.

Battery *SoC* is calculated according to Eq. (1).

$$SoC = SoC_0 - \frac{1}{Q_{\text{bat}}}\int_{t_0}^{t} I_{\text{bat}}\left(t\right)dt, \tag{1}$$

where Q_{bat} is the nominal capacity of the battery and equals 207 A h, I_{bat} the battery current, and SoC_0 the initial state of charge. The relation between the power measured at the terminal and the battery current can be formulated in Eq. (2):

$$P_{\text{bat}} = \left(V_{\text{oc,bat}} - V_{1,\text{bat}} - V_{2,\text{bat}} - V_{3,\text{bat}}\right)\cdot I_{\text{bat}} - I_{\text{bat}}^2\cdot R_{0,\text{bat}}, \tag{2}$$

where $R_{0,\text{bat}}$is the internal resistance of the battery, $V_{\text{oc,bat}}$ the open circuit voltage of the battery, $V_{1,\text{bat}}$, $V_{2,\text{bat}}$, and $V_{3,\text{bat}}$ the voltage across each R-C branch, respectively, as shown in Fig. 4. With introducing a variable in Eq. (3) that represents the difference between the open-circuit voltage and the parasitic voltages:

$$V_{\text{diff}} = V_{\text{oc,bat}} - V_{1,\text{bat}} - V_{2,\text{bat}} - V_{3,\text{bat}}, \tag{3}$$

the Eq. (2) can be rewritten as Eq. (4):

$$P_{\text{bat}} = V_{\text{diff}}\cdot I_{\text{bat}} - I_{\text{bat}}^2\cdot R_{0,\text{bat}}. \tag{4}$$

3. Adaptive Pontryagin's minimum principle-based strategy

3.1. Fundamentals of offline PMP

In general, an energy management strategy implemented in a hybrid electric vehicle is designed to minimize the fuel consumption, while fulfilling all dynamic power requirements imposed on the electric vehicle. In this section, the PMP algorithm is applied in energy management as the benchmark for the to be introduced APMP. The goal is to minimize hydrogen consumption, and the corresponding Hamiltonian function is defined in Eq. (5):

$$H\left(SoC\left(t\right), P_{\text{fc}}\left(t\right), \lambda\left(t\right), t\right) = \dot{m}_{\text{H}_2}\left(P_{\text{fc}}\left(t\right)\right) + \lambda\left(t\right)\dot{SoC}\left(t\right), \tag{5}$$

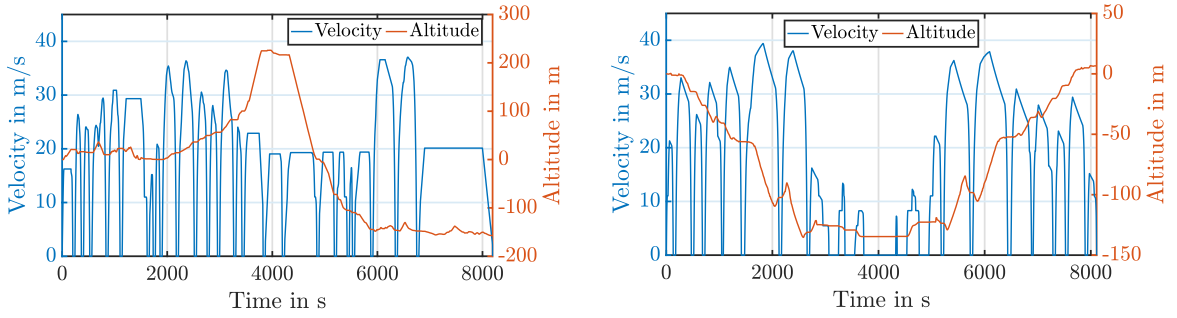

(a) ENV1. (b) ENV2.

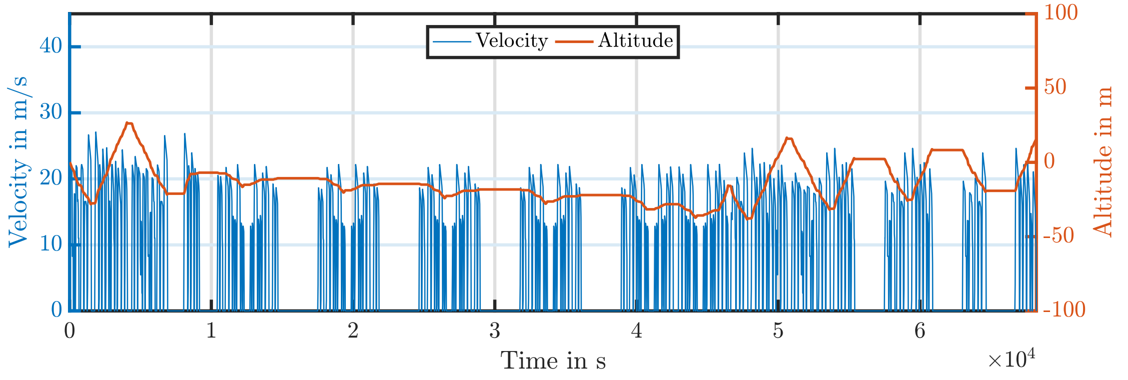

(c) ENV3.

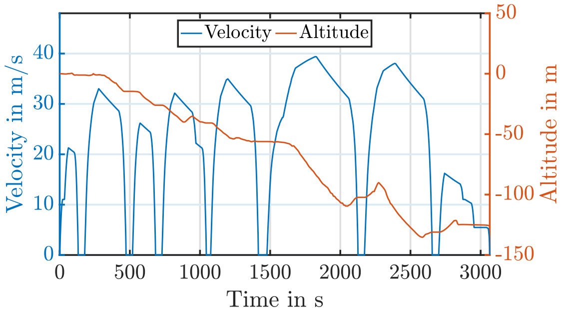

(d) ENV4.

Fig. 2. Velocity and altitude trajectories of different driving cycles.

Table 1
Parameters of driving cycles.

Driving cycle	Distance (km)	Travel time (s)
ENV1	145	8192
ENV2	145	8110
ENV3	584.5	68213
ENV4	70.2	3065

where $\dot{m}_{H_2}$ represents the mass flow of hydrogen and is a function of the fuel cell power. The SoC is the state variable, which is a subject of the following constraint in Eq. (5)

$$SoC_{\min} < SoC(t) < SoC_{\max}, \tag{6}$$

where $SoC_{\min}$ and $SoC_{\max}$ are the boundaries of permitted battery SoC range. In this application, they are assumed to be 0.15 and 0.9, as suggested by the supplier. Moreover, the fuel cell power is controlled within its constraints as shown in Eq. (7):

$$P_{\mathrm{fc,min}} < P_{\mathrm{fc}}(t) < P_{\mathrm{fc,max}}, \tag{7}$$

where $P_{\mathrm{fc,min}}$ and $P_{\mathrm{fc,max}}$ are the boundaries of permitted fuel cell power range. In this application, they are assumed to be 20 kW and 180 kW, respectively, to prolong its lifetime. The necessary conditions of the PMP-based strategy are formulated according to the optimal control theory in Eqs. (8)–(10):

$$P^{*}_{\mathrm{fc}}\left(t\right) = \underset{P_{\mathrm{fc}}\left(t\right)}{\mathrm{argmin}}\left(H\left(SoC\left(t\right),P_{\mathrm{fc}}\left(t\right),\lambda\left(t\right),t\right)\right), \tag{8}$$

$$\dot{SoC}\left(t\right) = \frac{\partial}{\partial\lambda}H\left(SoC\left(t\right),P_{\mathrm{fc}}\left(t\right),\lambda\left(t\right),t\right), \tag{9}$$

$$\dot{\lambda}\left(t\right) = -\frac{\partial}{\partial SoC}H\left(SoC\left(t\right),P_{\mathrm{fc}}\left(t\right),\lambda\left(t\right),t\right). \tag{10}$$

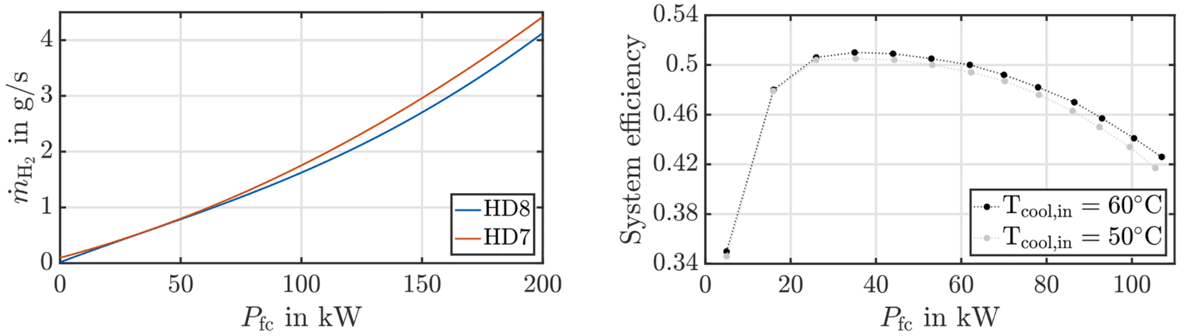

(a) Specific consumption curve of different fuel cell products: *HD7* and *HD8*.

(b) Dependency of *HD7* efficiency on Temperature.

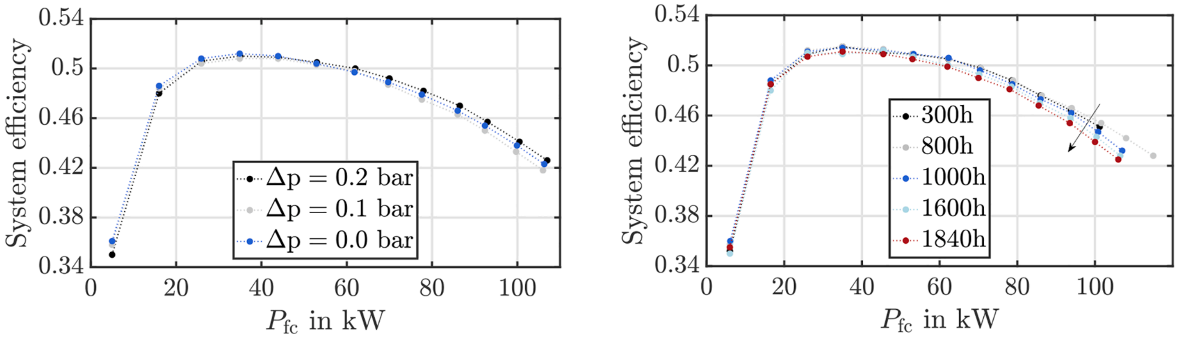

(c) Dependency of *HD7*'s efficiency on pressure difference.

(d) Dependency of *HD7*'s efficiency on operational hours.

Fig. 3. Dependency of fuel cell system efficiency on various factors.

Table 2
Battery parameters.

Parameters	Value	Units
Nominal voltage	850	V
Voltage range	760 ~ 950	V
Nominal capacity	207	Ah
Recommended SoC range	0.15 ~ 0.95	–

Since the train in this application works under charge-sustaining condition, the SoC end value is equal to its initial value as Eq. (11) shows:

$$SoC(t_f) = SoC_{target} = SoC_0. \tag{11}$$

According to the equivalent electrical circuit of the battery, the battery current I_{bat}related to the load power and fuel cell power can be represented in Eq. (12):

$$I_{bat} \cdot (V_{diff} - R_{0,bat} \cdot I_{bat}) = P_{load} - P_{fc}. \tag{12}$$

The battery current can be written in the function of the load power and the fuel cell power as shown in Eq. (13):

$$I_{bat} = \frac{V_{diff}}{2R_{0,bat}} - \frac{\sqrt{(V_{diff})^2 - 4(P_{load} - P_{fc})R_{0,bat}}}{2R_{0,bat}} \tag{13}$$

The $V_{1,bat}$, $V_{2,bat}$, and $V_{3,bat}$included in V_{diff}, vary as shown in the following first-order differential equations:

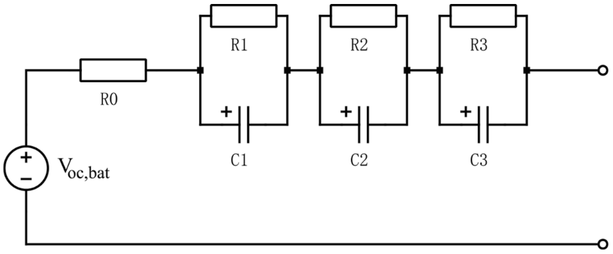

Fig. 4. Third-order equivalent electrical circuit of the battery system.

$$\begin{aligned}
\dot{V}_{1,bat} &= -\frac{V_{1,bat}}{R_{1,bat} \cdot C_{1,bat}} + \frac{1}{C_{1,bat}} \cdot I_{bat}, \\
\dot{V}_{2,bat} &= -\frac{V_{2,bat}}{R_{2,bat} \cdot C_{2,bat}} + \frac{1}{C_{2,bat}} \cdot I_{bat}, \\
\dot{V}_{3,bat} &= -\frac{V_{3,bat}}{R_{3,bat} \cdot C_{3,bat}} + \frac{1}{C_{3,bat}} \cdot I_{bat},
\end{aligned} \tag{14}$$

where $R_{1,bat}$, $R_{2,bat}$, $R_{3,bat}$ and $C_{1,bat}$, $C_{2,bat}$, $C_{3,bat}$ are the resistances and capacitances of each RC branch, all of which are functions of SoC. Then, the dynamics of state can be calculated as follows:

$$\dot{SoC}\left(t\right) = -\frac{V_{diff}}{2R_{0,bat}Q_{bat}} + \frac{\sqrt{(V_{diff})^2 - 4(P_{load} - P_{fc})R_{0,bat}}}{2R_{0,bat} \cdot Q_{bat}}. \tag{15}$$

The battery open-circuit voltage $V_{oc,bat}$ and the internal resistance $R_{0,bat}$ are SoC-dependent. Therefore, the dynamic of the state variable is indirectly related to SoC, and the dynamic of the costate λ in Eq. (10) can be reformulated as follows:

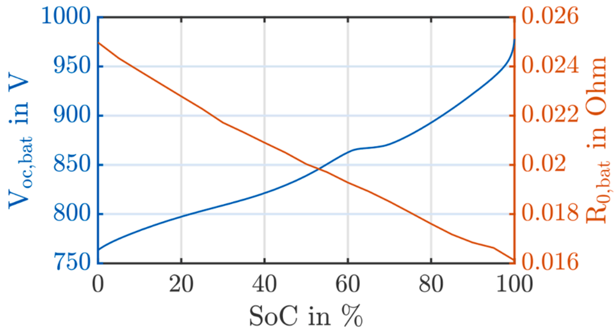

Fig. 5. Open-circuit voltage and internal resistance of the battery system under Temperature of 25 °C.

$$\dot{\lambda}(t) = -\lambda\cdot\frac{\partial \dot{SoC}}{\partial SoC} = -\lambda\cdot\left(\frac{\partial \dot{SoC}}{\partial V_{\mathrm{oc,bat}}}\frac{\partial V_{\mathrm{oc,bat}}}{\partial SoC} + \frac{\partial \dot{SoC}}{\partial V_{1,\mathrm{bat}}}\frac{\partial V_{1,\mathrm{bat}}}{\partial SoC} + \frac{\partial \dot{SoC}}{\partial V_{2,\mathrm{bat}}}\frac{\partial V_{2,\mathrm{bat}}}{\partial SoC} + \frac{\partial \dot{SoC}}{\partial V_{3,\mathrm{bat}}}\frac{\partial V_{3,\mathrm{bat}}}{\partial SoC} + \frac{\partial \dot{SoC}}{\partial R_{0,\mathrm{bat}}}\frac{\partial R_{0,\mathrm{bat}}}{\partial SoC}\right). \tag{16}$$

However, only the SoC can change freely, and other variables such as $V_{1,\mathrm{bat}}$, $V_{2,\mathrm{bat}}$, and $V_{3,\mathrm{bat}}$, change depending on the history of the variable SoC, because the change rate of the SoC and the voltage over the parasitic capacitors are coupled by the battery current. Therefore, only the SoC is defined as the state variable, while the voltages over three R-C branches are observed as variable parameters. These variable parameters are updated in each time instant. As a result, the partial derivatives of $V_{1,\mathrm{bat}}$, $V_{2,\mathrm{bat}}$, and $V_{3,\mathrm{bat}}$ with respect to the SoC are assumed to be zero as follows:

$$\frac{\partial V_{1,\mathrm{bat}}}{\partial SoC} = \frac{\partial V_{2,\mathrm{bat}}}{\partial SoC} = \frac{\partial V_{3,\mathrm{bat}}}{\partial SoC} = 0, \tag{17}$$

and Eq. (16) can be derived as:

$$\dot{\lambda}\left(t\right) = -\lambda\cdot\left(\frac{\partial \dot{SoC}}{\partial V_{\mathrm{oc,bat}}}\cdot\frac{\partial V_{\mathrm{oc,bat}}}{\partial SoC} + \frac{\partial \dot{SoC}}{\partial R_{0,\mathrm{bat}}}\cdot\frac{\partial R_{0,\mathrm{bat}}}{\partial SoC}\right). \tag{18}$$

The partial derivative of the dynamic of the state variable with respect to the open-circuit voltage results as:

$$\frac{\partial \dot{SoC}}{\partial V_{\mathrm{oc,bat}}} = -\frac{1}{2R_{0,\mathrm{bat}}Q_{\mathrm{bat}}}\cdot\left(1-\frac{V_{\mathrm{diff}}}{\sqrt{V_{\mathrm{diff}}^2-4\left(P_{\mathrm{load}}-P_{\mathrm{fc}}\right)R_{0,\mathrm{bat}}}}\right), \tag{19}$$

and the derivation of the SoC dynamic with respect to the battery resistance as:

$$\frac{\partial \dot{SoC}}{\partial R_{0,\mathrm{bat}}} = \frac{1}{2R_{0,\mathrm{bat}}^2Q_{\mathrm{bat}}}\left(\frac{2\left(P_{\mathrm{load}}-P_{\mathrm{fc}}\right)R_{0,\mathrm{bat}}-V_{\mathrm{diff}}^2}{\sqrt{V_{\mathrm{diff}}^2-4\left(P_{\mathrm{load}}-P_{\mathrm{fc}}\right)R_{0,\mathrm{bat}}}}+V_{\mathrm{diff}}\right). \tag{20}$$

Using the derivations provided above, the optimal control problem can be executed based on the PMP algorithm. At each time instant over the optimization horizon, under the required load power, the Hamiltonian is computed and minimized based on Eq. (8). As a result, the optimized control variable P_{fc} is determined and then applied to the state and the costate dynamic equations to update the values of the state and the costate in the next discrete time instant. The calculation process iterates until the end of the drive time. The initial values of the costate and the state variable are required to start this iterative process. However, only the initial state and end value of state are known and the initial value of the costate is physically not available, from which the name of two-point boundary value problem comes. Since the system is not linear, this two-point boundary value problem can only be solved numerically through an iterative procedure. For that purpose, the shooting method based on a bidirectional search is utilized to find the right initial costate [10]. Fig. 6 shows the SoC and the costate trajectories depending on the initial value of the costate. It is evident that the results of PMP are strongly sensitive to the initial value of the costate λ, which is the most critical issue for real-time application.

It is worth mentioning that by applying the PMP as the benchmark, the load power trajectory and the SoC initial and end values resulted from the online strategies are used as input for the PMP algorithm.

3.2. Analytical derivation of the costate

According to the offline PMP from the previous section, the results are strongly sensitive to the initial estimate of the costate. Therefore, the shooting method is applied for finding the proper initial value of costate. However, the shooting method requires knowledge of the driving cycle in advance and therefore is not suitable for real-time application. In this section, to eliminate the sensitivity of the PMP strategy depending on the estimation of the costate initial value, a new analytical method is developed to correct the costate during the real-time operation.

The formulation of the Hamiltonian function, as already shown in Eq. (5), plays a central role in analytically correcting the costate. Physically, the costate λ represents the equivalent amount of hydrogen consumption for using battery power. According to the PMP results of fuel cell power in Fig. 7, the optimal operation points of fuel cell power are mostly near their average value.

Due to the charge-sustaining condition, considering the energy conservation law, the total electrical energy generated from fuel cell should fully cover the total load energy and the total energy loss in the battery as follows:

$$\int_{t_0}^{t_f} P_{\mathrm{fc}}\left(t\right)dt = \int_{t_0}^{t_f}\left(P_{\mathrm{load}}\left(t\right)+P_{\mathrm{loss,bat}}\left(t\right)\right)dt, \tag{21}$$

and the average power is defined as follows:

$$\overline{P}_{\mathrm{fc}} = \frac{\int_{t_0}^{t_f} P_{\mathrm{fc}}\left(t\right)dt}{T}, \overline{P}_{\mathrm{load}} = \frac{\int_{t_0}^{t_f} P_{\mathrm{load}}\left(t\right)dt}{T}, \overline{P}_{\mathrm{loss,bat}} = \frac{\int_{t_0}^{t_f} P_{\mathrm{loss,bat}}\left(t\right)dt}{T}, \tag{22}$$

where T is the total travel time defined as:

$$T = t_f - t_0. \tag{23}$$

Then, Eq. (21) is divided by T on both sides, to gain the relation that regards the average power values:

$$\overline{P}_{\mathrm{fc}} = \overline{P}_{\mathrm{load}} + \overline{P}_{\mathrm{loss,bat}}, \tag{24}$$

which means the DC component of the fuel cell power (average value) fully covers the load demand and the battery losses. Therefore, not all the fuel cell power participates in energy conservation into the battery. The equivalent amount of hydrogen mass for using battery power, which the costate λ represents, is merely related to the incremental part of the fuel cell power. In conclusion, only the incremental part of hydrogen flow and the dynamics of SoC should be considered to derive the costate λ, which is depicted as follows:

$$\Delta P_{\mathrm{fc}} = \Delta \dot{SoC}\cdot\overline{V}_{\mathrm{oc,bat}}\cdot Q_{\mathrm{bat}}. \tag{25}$$

By linearizing the specific consumption curve of the fuel cell at the average operation point, as shown in the Fig. 8, follows the relation between the incremental fuel cell power and the incremental hydrogen consumption as:

$$\Delta P_{\mathrm{fc}} = \Delta \dot{m}_{\mathrm{H_2}} \Big/ \frac{\partial \dot{m}_{\mathrm{H_2}}}{\partial P_{\mathrm{fc}}}\Big|_{\mathrm{P_{fc}=\overline{P}_{fc}}}, \tag{26}$$

which can be substituted into Eq. (25), then

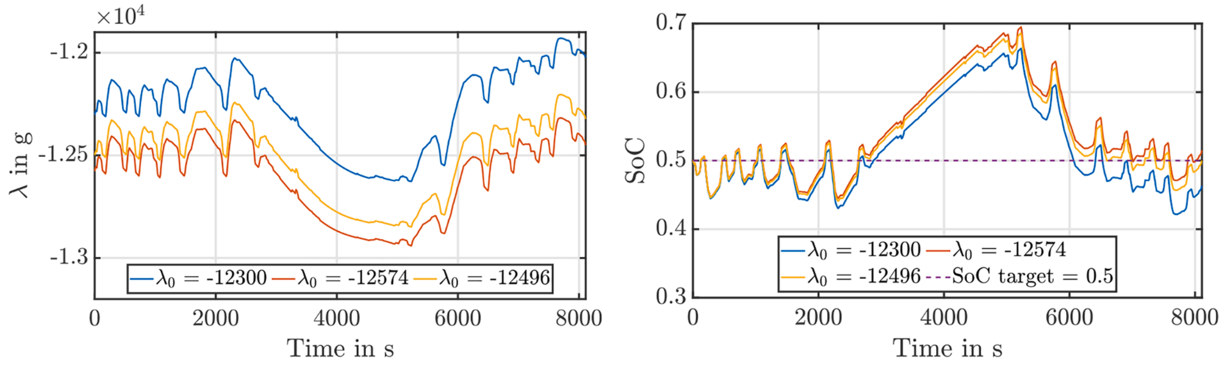

(a) The influence of λ_0 on $\lambda(t)$ trajectories. (b) The influence of λ_0 on $SoC(t)$ trajectories.

Fig. 6. The influence of λ_0 on PMP results.

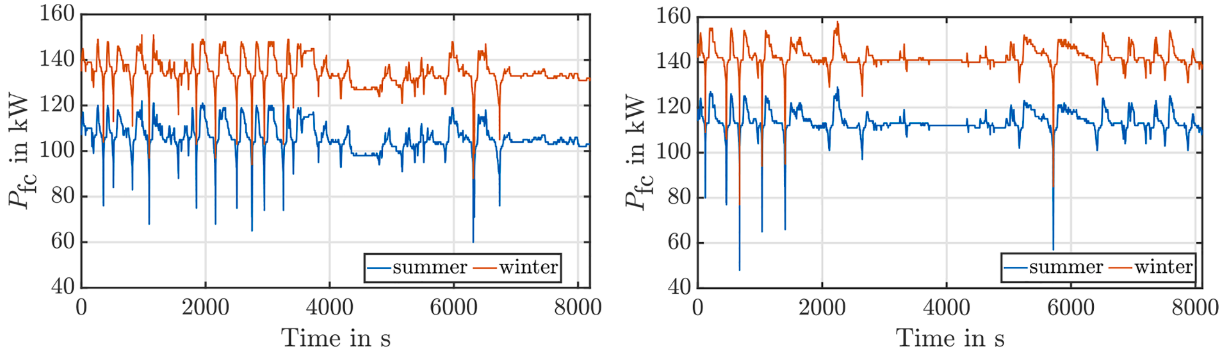

(a) ENV1. (b) ENV2.

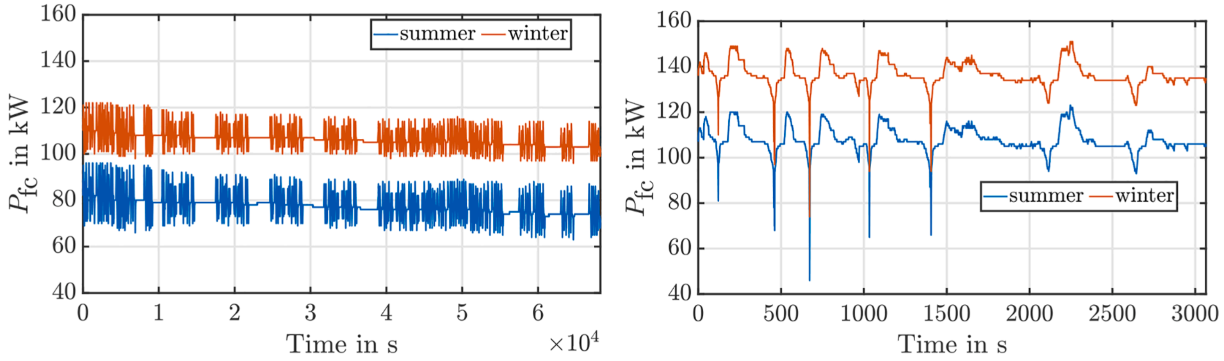

(c) ENV3. (d) ENV4.

Fig. 7. P_{fc} trajectories resulted from PMP regarding different driving cycles.

$$\Delta \dot{m}_{H_2} \Big/ \frac{\partial \dot{m}_{H_2}}{\partial P_{fc}}\Big|_{P_{fc}=\overline{P}_{fc}} = \Delta \dot{SoC}\cdot \overline{V}_{oc,bat}\cdot Q_{bat}. \tag{27}$$

Due to the energy conservation principle, an increase in battery power leads to hydrogen consumption. As a result, the costate λ is derived as:

$$\lambda = -\frac{\Delta \dot{m}_{H_2}}{\Delta \dot{SoC}} = -\overline{V}_{oc,bat}\cdot Q_{bat}\cdot \frac{d\dot{m}_{H_2}}{dP_{fc}}\Big|_{P_{fc}=\overline{P}_{fc}}. \tag{28}$$

It is evident that the costate λ is a function of SoC included in the open-circuit voltage $V_{oc,bat}$, and of the average fuel cell power $\overline{P}_{fc}$, which is related to the derivative of the mass flow with respect to the fuel cell power. According to the equation, the costate can be plotted as the function of SoC and the average fuel cell power, as shown in Fig. 9. After comparison to the curve from the offline results, the effectiveness of the analytical formula is validated.

The analytical Eq. (28) requires several parameters regarding the characteristics of the fuel cell system and battery system, which are merely related to the components themselves, and independent from specific driving cycles. Therefore, this analytical formulation of estimating the costate guarantees the causality of the APMP strategy for online applications, and it also has adaptivity to be scaled or transferred to other system configurations without the loss of effectiveness. Even in the case of component degradation, this analytical formula automatically adapts itself regarding the actual component characteristics to maintain its accuracy, which will be verified through simulation results in the followed section.

The prerequisite of using Eq. (28) to correct the costate λ is a

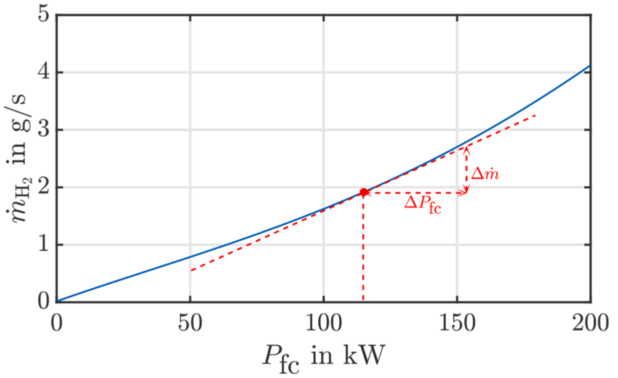

Fig. 8. Linearization of the fuel cell's specific consumption curve at the average operation point, where $\Delta\dot{m}$ represents the incremental mass flow at the linearized point, and ΔP_{fc} the incremental fuel cell power.

reasonable estimation of average fuel cell power $\overline{P}_{fc}$ along the whole driving cycle, which is, however, challenging in real-time applications. For that purpose, an accurate estimation of the average fuel cell power will be introduced in the next section. Summarily, the equation Eq. (28) is utilized regularly to correct the costate, and in remaining periods, the costate λ evolves through its dynamic, as shown in Eq. (16), to achieve the best local optimality based on PMP.

Then, the remaining crucial tasks for APMP strategy are how to accurately estimate the average fuel cell power along the whole driving cycle and when to update the costate analytically. Further correction of the average fuel cell power based on the timetable and the plug-in operation, is not the focus of this work, and can be found in [11].

3.3. Estimation of the fuel cell average power

The estimation of the average fuel cell power is fundamentally based on the historical operation status of the train. Typically, a vast amount of positive load power is demanded during the acceleration phase, and negative power is recuperated during the regenerative braking phase. Therefore, the average fuel cell power is overestimated during acceleration and underestimated during regenerative braking. In this work, the time instant, when the train leaves each station, is chosen to update the average fuel cell power and average battery loss, as shown in the following Fig. 10:

In this way, the average fuel cell power is estimated to be:

$$\overline{P}_{fc}\left(t\right) = \frac{\int_{t_0}^{t} P_{load}\left(t\right)d\tau + \int_{t_0}^{t} P_{loss,bat}\left(t\right)d\tau}{t}, \tag{29}$$

whereby the load power P_{load} is the sum of various power as:

$$P_{load}(t) = P_{trac} + P_{loss,driveline}(t) + P_{auxiliary}, \tag{30}$$

where P_{trac} represents the traction power, $P_{loss,driveline}$ various power losses along the drive-line, and $P_{auxiliary}$ the auxiliary consumption.

4. Robustness analysis of APMP based on simulation

4.1. APMP without components aging

In this part, the trajectories resulted from the APMP-based strategy for different driving cycles and weather conditions are displayed, together with those resulted from PMP. The power consumption of auxiliary units in winter is about 30 kW higher than in summer due to air

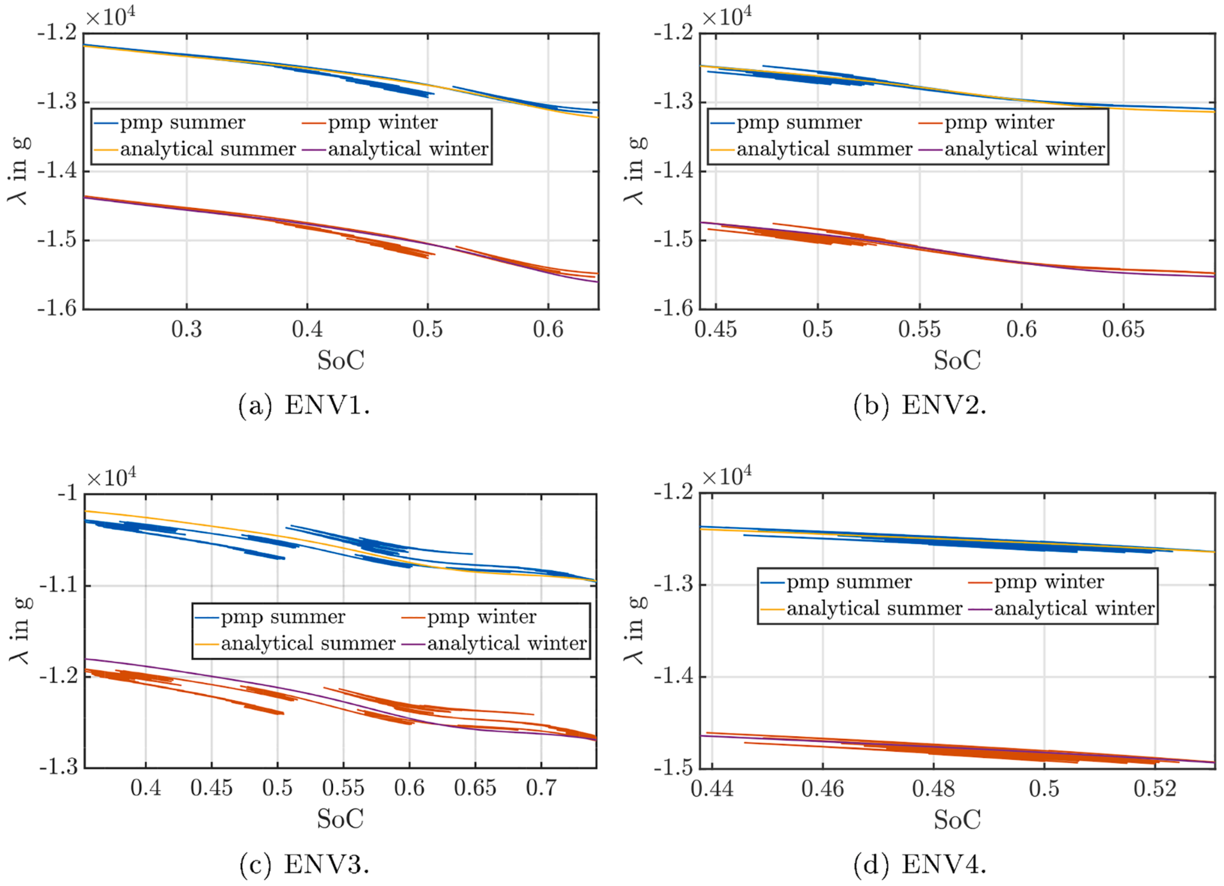

(a) ENV1.

(b) ENV2.

(c) ENV3.

(d) ENV4.

Fig. 9. Costate trajectories as the function of SoC regarding different driving cycles.

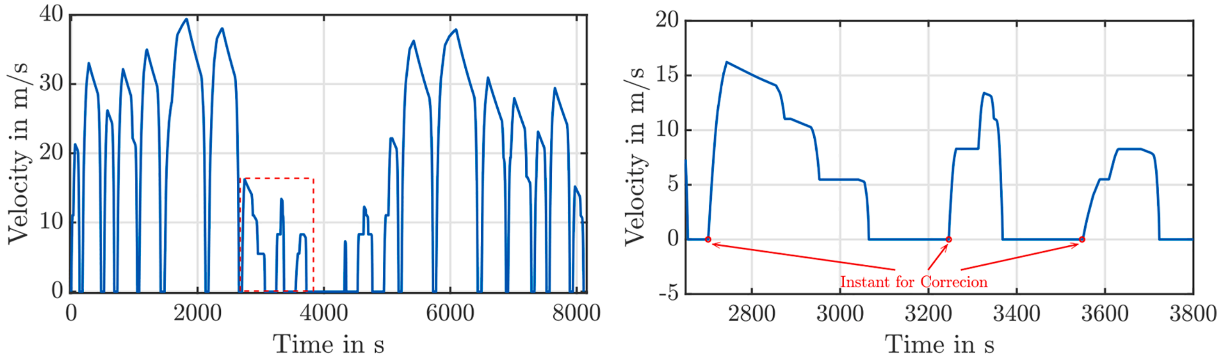

(a) Global view.
(b) Zoom in view.

Fig. 10. Time instant to update the average fuel cell power and average battery loss.

conditioning. The initial SoC is 0.5 for all simulations, and the fuel cell system *HD8* is used.

Based on the method of estimating the average fuel cell power from the previous section, trajectories of estimated average fuel cell power in comparison to global average value under different driving cycles with various weather conditions are shown in Fig. 11. The trajectory of estimated average fuel cell power under the driving cycle ENV3 almost overlaps with its global average value, while those under other driving cycles have more deviations. The degree of the relative deviations is formulated as

$$\overline{\Delta P_{\text{fc,aver}}} = \frac{\int_{t_0}^{t_f} \left| P_{\text{fc,aver,esti}}\left(t\right) - P_{\text{fc,aver,global}} \right| dt}{T}, \tag{31}$$

where $P_{\text{fc,aver,esti}}(t)$ is the varied estimate of the average fuel cell power by using Eq. (29) and $P_{\text{fc,aver,global}}$ the average power along the entire driving cycles, which are also collected in Table 3. The reason for the small deviation is that the driving cycle ENV3 has much longer traveling time and more stations. Based on more historical data, the error of estimation can be corrected in time. Although there are such large deviations under the other three driving cycles in the short-time scale, the positive and negative deviations are compensated against each other which does not overly affect the charge-sustaining condition.

The corresponding SoC trajectories are shown in Fig. 12. They nearly overlap with the PMP results under all driving cycles for different weather conditions. Even though the charge-sustaining mode is not strictly achieved, as shown in Table 3, they will be compensated in another subsequent trip.

Based on the proper estimation of average fuel cell power, the costate λ is also analytically well estimated. Since the average fuel cell power is

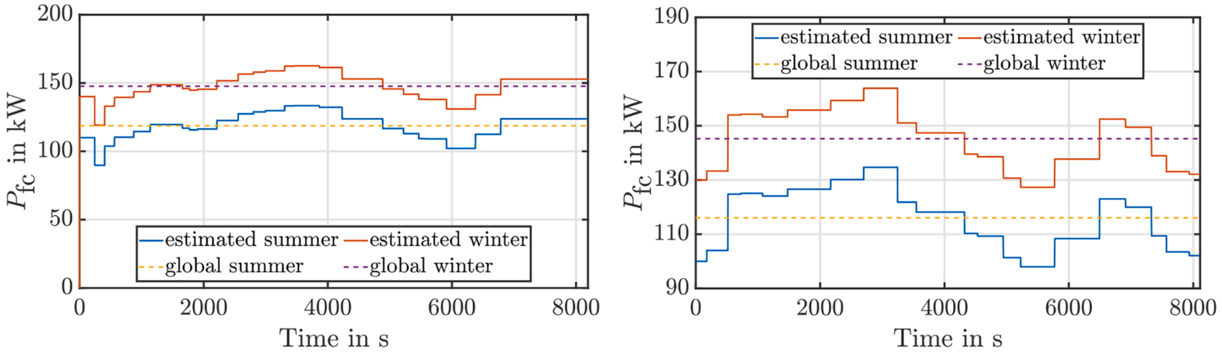

(a) ENV1.
(b) ENV2.

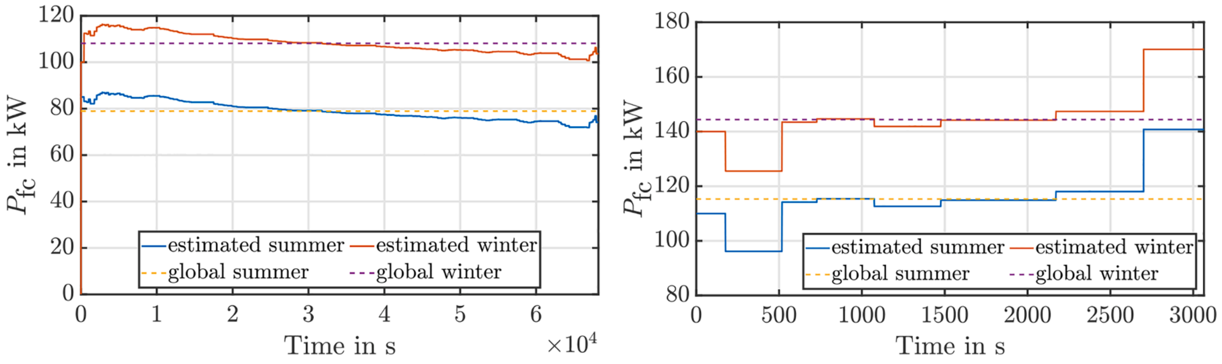

(c) ENV3.
(d) ENV4.

Fig. 11. Trajectories of estimated average fuel cell power in comparison to global average value under different driving cycles for various weather conditions.

Table 3
Simulation results of APMP.

Driving cycle		1	2	3	4
Summer	$\overline{\Delta P}_{\mathrm{fc,aver}}$	6.53%	8.39%	4.2%	5.75%
	$\mathbf{SoC_{end}}$	0.64	0.52	0.58	0.53
	$\bar{\lambda}$ (g)	−12853	−12910	−10748	−12625
	Ref.$\lvert\bar{\lambda}\rvert$ PMP	+4.68%	+5.59%	+1.35%	+3.86%
	$\mathrm{m_{H_2}}$ (g)	32726	31554	170724	11836
	$\mathrm{m_{H_2}}$ (g/km)	212.39	216.39	292.08	168.62
	Ref.$\mathrm{m_{H_2}}$	+2.13%	+1.48%	+0.59%	+1.72%
Winter	$\overline{\Delta P}_{\mathrm{fc,aver}}$	5.27 (%)	6.66%	3.09%	4.58%
	$\mathbf{SoC_{end}}$	0.64	0.52	0.63	0.53
	$\bar{\lambda}$ (g)	−15172	−15257	−12507	−14917
	Ref.$\lvert\bar{\lambda}\rvert$	+4.68%	+4.68%	+1.75%	+3.87%
	$\mathrm{m_{H_2}}$ (g)	43464	42102	242934	15800
	$\mathrm{m_{H_2}}$ (g/km)	282.07	288.73	415.62	225.09
	Ref.$\mathrm{m_{H_2}}$	+1.91%	+1.33%	+0.48%	+1.57%

the only crucial input parameter for the estimation of the costate λ, the accuracy of the estimations is bonded to each other. As shown in Fig. 13, the trajectories of the costate λ in APMP are basically around those in the PMP results. Especially under the driving cycle ENV3, the result shows a high degree of coincidence, while regarding the results under the other three driving cycles, the degree of coincidence is lower, which is consistent with the result of estimated average fuel cell power in Fig. 11. The average relative deviations of the costate λ under each driving cycle are listed in Table 3.

The trajectories of fuel cell power are displayed in Fig. 14 as the final output of the APMP-based strategy. They strongly overlap with the PMP results under all driving cycles in each weather condition. Since the highest degree of coincidence in the estimated average fuel cell power and the costate λ is achieved for the driving cycle ENV3, the fuel cell trajectory also shows an outstanding consistency with PMP results, which is also intuitively reflected in fuel economy. As shown in Table 3, under the driving cycle ENV3, the hydrogen consumption is higher for 0.59% in summer and 0.48% in winter time, compared to the results of PMP, respectively, which is significantly lower than the other three driving cycles. The additional hydrogen consumption under the other three driving cycles is up to 2.13% for the driving cycle ENV1 in summer.

4.2. APMP with fuel cell aging accurately monitored

The influence of aging on the fuel cell system is directly reflected in its specific consumption curve and efficiency curve. The specific consumption curve of the fuel cell system *HD8* after aging is not available, because it requires a long operation period. Therefore, the specific consumption curve of another fuel cell system named *HD7* of Ballard at the beginning and the end of the lifetime are used to test the robustness of the APMP-based strategy under fuel cell aging. They are fitted respectively according to the given data sheet from Ballard by using second-order polynomial as follows:

$$\begin{aligned}\dot{m}_{\mathrm{H_2,HD7}} &= 0.1387\cdot P_{\mathrm{fc}}^2 + 1.244\cdot P_{\mathrm{fc}} + 1.6,\\ \dot{m}_{\mathrm{H_2,HD7Aging}} &= 0.1985\cdot P_{\mathrm{fc}}^2 + 1.318\cdot P_{\mathrm{fc}} + 1.626,\end{aligned} \tag{32}$$

as shown in Fig. 15(a). The first-order differentiation curves are shown in Fig. 15(b).

It is assumed that the specific consumption curve of the fuel cell after aging is estimated accurately. The APMP simulation results under the driving cycle ENV2 are displayed in the Fig. 16, together with the results of the PMP strategy as the benchmark, with the same aging degree considered. It is worth mentioning that the conclusions under the

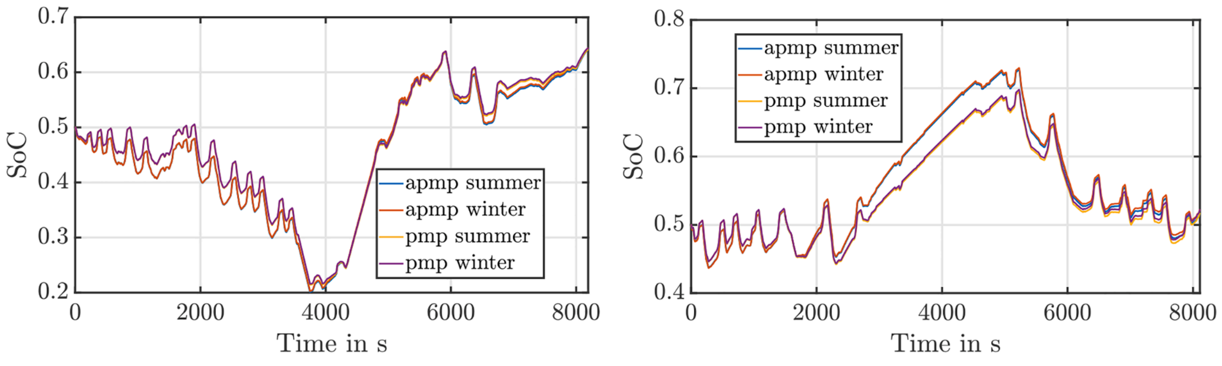

(a) ENV1. (b) ENV2.

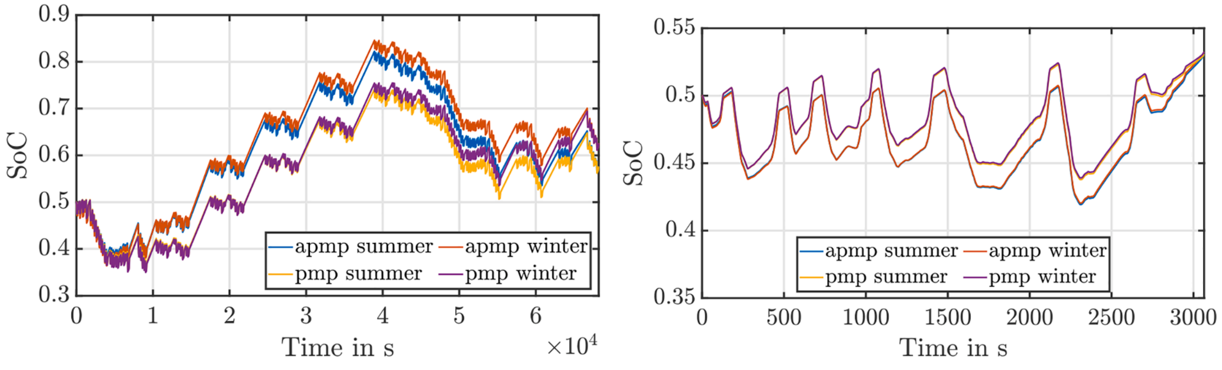

(c) ENV3. (d) ENV4.

Fig. 12. SoC trajectories of APMP results in comparison to PMP results under different driving cycles for various weather conditions.

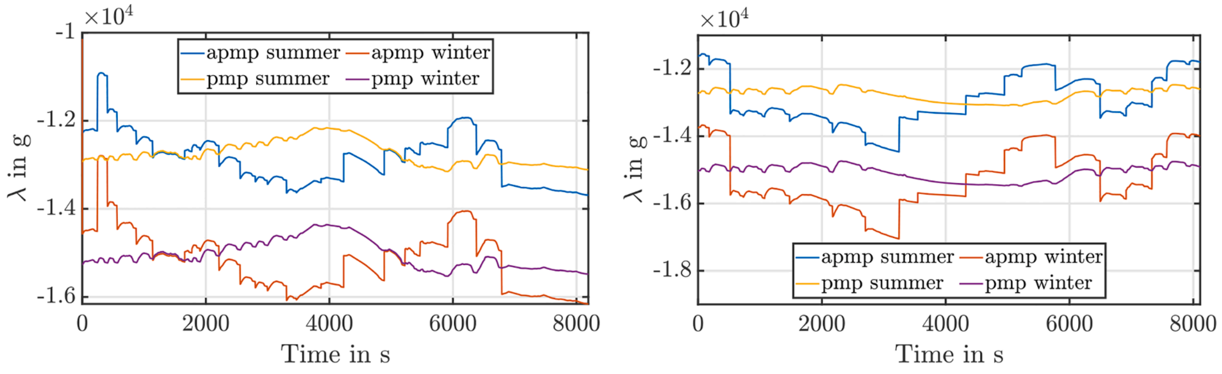

(a) ENV1. (b) ENV2.

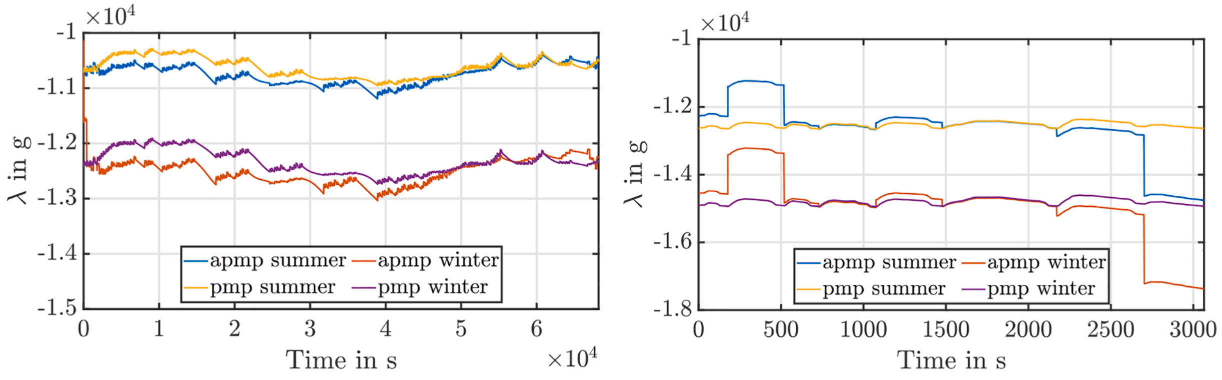

(c) ENV3. (d) ENV4.

Fig. 13. λ trajectories of APMP results in comparison to PMP results under different driving cycles for various weather conditions.

driving cycle ENV2 can be transferred to other driving conditions. It is evident that the fuel cell power and SoC trajectories from simulations, which use the original model or the aging model for the fuel cell system, are similar for both PMP results in Fig. 16(a) and (c) and APMP results in Fig. 16(b) and (d). This proves the excellent adaptivity of the strategy. As shown in Fig. 16(e) and (f), the trajectory of $\lambda(t)$ has similar trends but is increased in amplitude in case the aging process is considered, for both PMP and APMP results. The reason lies in the decreased efficiency of the fuel cell system with aging increased. Regarding the same power demand, the same increase of SoC causes higher hydrogen consumption. Therefore, the amplitude of $\lambda(t)$ increases.

The costate λ is evaluated with its average relative deviation of 0.84% and 0.82% in reference to the PMP results, for summer and winter conditions, respectively, as shown in Table 4. It is worth mentioning that the average relative deviation of $\lambda(t)$ increases negligibly compared to the case without fuel cell aging. In Table 4, the important parameters related to fuel economy are listed. With fuel cell aging considered, the additional hydrogen consumption in comparison to PMP results is 1.47% and 1.23%, for summer and winter, respectively, which are slightly increased compared to the case without fuel cell aging. By comparing hydrogen consumption between cases with and without aging, merely slight increase is observed. As a conclusion, the APMP-based strategy maintains its performance after fuel cell aging, which shows low sensitivity and high degree of robustness.

4.3. APMP with battery aging accurately monitored

Here, without explanation of the battery aging mechanism, it is assumed that a capacitance loss of 10% and an internal resistance increase of 5% occur:

$$\begin{aligned} Q_{\text{bat,aging}} &= 0.9 \cdot Q_{\text{bat}}, \\ R_{0,\text{bat,aging}} &= 1.05 \cdot R_{0,\text{bat}}. \end{aligned} \tag{33}$$

Furthermore, it is assumed that the internal resistance and capacity of the battery after aging can be estimated accurately. The APMP simulation results under the driving cycle ENV2 are displayed in the Fig. 17, and PMP results with the same aging degree considered are set as the benchmark for the APMP results. The fuel cell power trajectory under the original battery model and the aging model are almost the same for both the PMP results in Fig. 17(a) and the APMP results in Fig. 17(b). However, the SoC trajectories in Fig. 17(c) and (d) show a clear gap between the original model and the aging model. The reason lies in the decreased capacitance of the battery. With aging considered, the depth of battery discharge is more than the one without aging considered. The trajectories of the costate λ in Fig. 17(e) and (f) have similar trends, and the amplitude is decreased after the aging process. Due to the lower battery capacity after aging, the same increase of SoC corresponds to less battery power consumption, which means less hydrogen consumption. Therefore the amplitude of the costate λ goes down.

As shown in Table 5, the costate λ is evaluated with its average relative deviation of 1.24% and 1.15% in reference to the PMP results, for summer and winter conditions, respectively. The average relative deviation of $\lambda(t)$ increases slightly compared to the case without battery aging. The fuel economy with battery aging considered is displayed in Table 5. The additional hydrogen consumption in comparison to the PMP results is 1.50% and 1.36%, for summer and winter, respectively, which are slightly increased compared to the case without battery aging. By comparing hydrogen consumption between cases with and without battery aging through PMP or APMP based strategy, a slight increase is observed. The reason lies in the relatively high internal resistance of

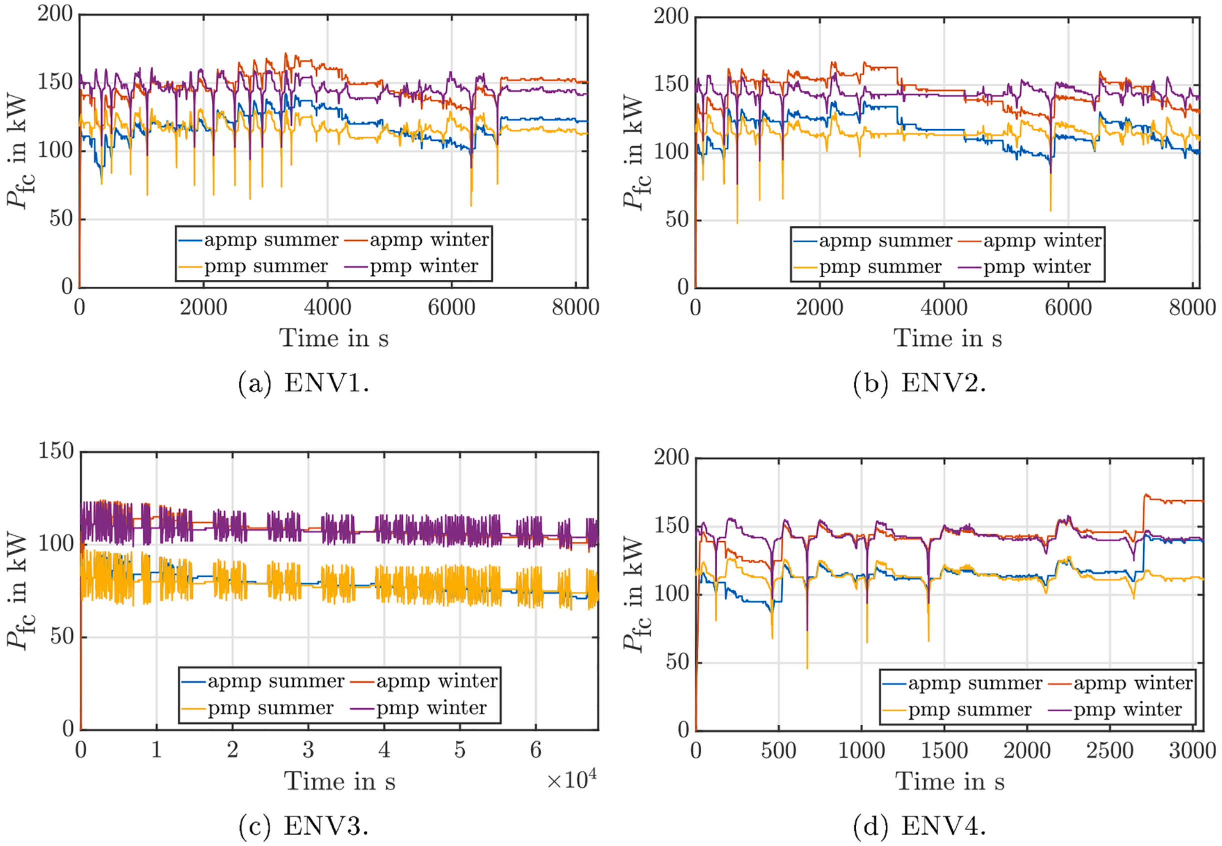

(a) ENV1.

(b) ENV2.

(c) ENV3.

(d) ENV4.

Fig. 14. P_{fc} trajectories of APMP results in comparison to PMP results under different driving cycles for various weather conditions.

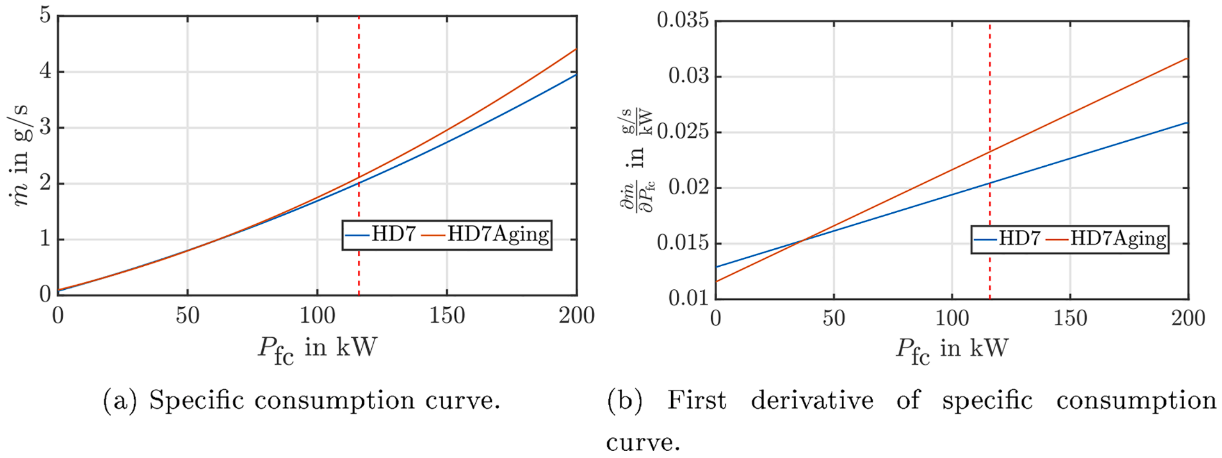

(a) Specific consumption curve.

(b) First derivative of specific consumption curve.

Fig. 15. Aging property of the fuel cell system *HD7*.

battery after aging and, therefore, more dissipated energy. All in all, the APMP-based strategy maintains its excellent fuel economy after battery aging, which shows low sensitivity and a high degree of robustness.

4.4. APMP with inaccurate fuel cell modeling

In the case of component aging previously, the characteristic curves of components are assumed to be estimated accurately if the aging degree increases. The PMP strategy results with the same aging degree considered are used as the benchmark for the APMP results. However, highly accurate estimation is challenging. Now, the robustness of the APMP strategy under inaccurate modeling of the fuel cell system is analyzed. Thereby, the specific consumption curve of the fuel cell system *HD8* used in the test bench is considered as the accurate modeling, while the curves of the fuel cell system *HD7* and the aged fuel cell system *HD7Aging* are considered as the inaccurate modeling of the fuel cell system. The results of the PMP-based strategy with the specific curve of the *HD8* applied are considered as the benchmark for the APMP results. Here, only the driving cycle ENV2 is tested.

Fig. 18 shows the simulation results of the PMP and the APMP strategy. The fuel cell power, SoC, and the costate trajectories resulted from the APMP-strategy, separately using the specific consumption curves of *HD8*, *HD7*, and *HD7Aging* to estimate the costate, are displayed in the right sub-figures in Fig. 18. The fuel cell power and the SoC trajectories under the APMP strategy with different specific consumption curves used are almost identical, as shown in Fig. 18(b) and (d). The

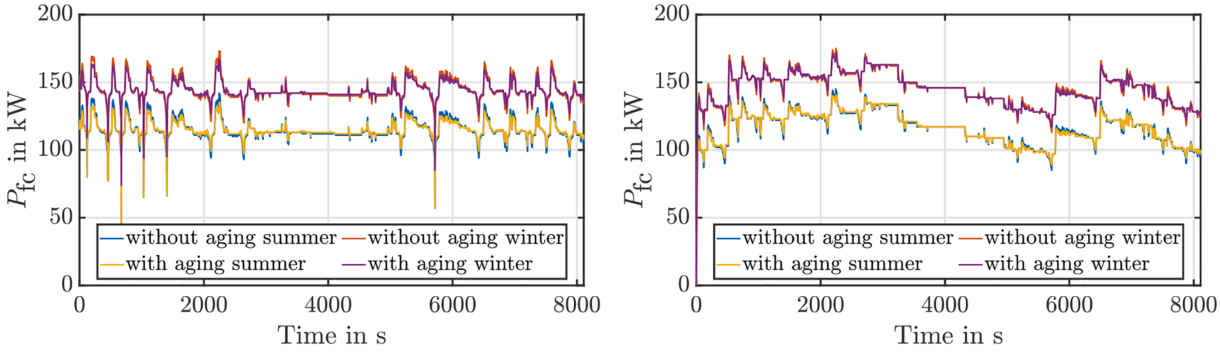

(a) $P_{fc}(t)$ trajectory from PMP results.

(b) $P_{fc}(t)$ trajectory from APMP results.

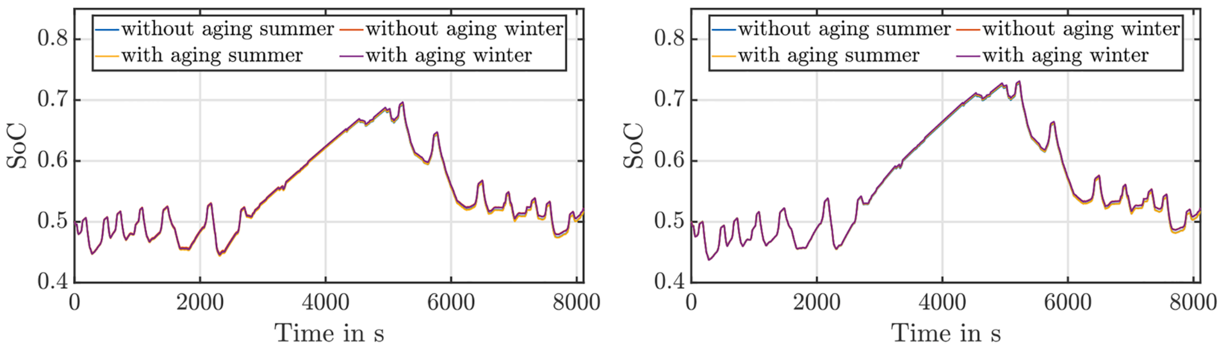

(c) $SoC(t)$ trajectory from PMP results.

(d) $SoC(t)$ trajectory from APMP results.

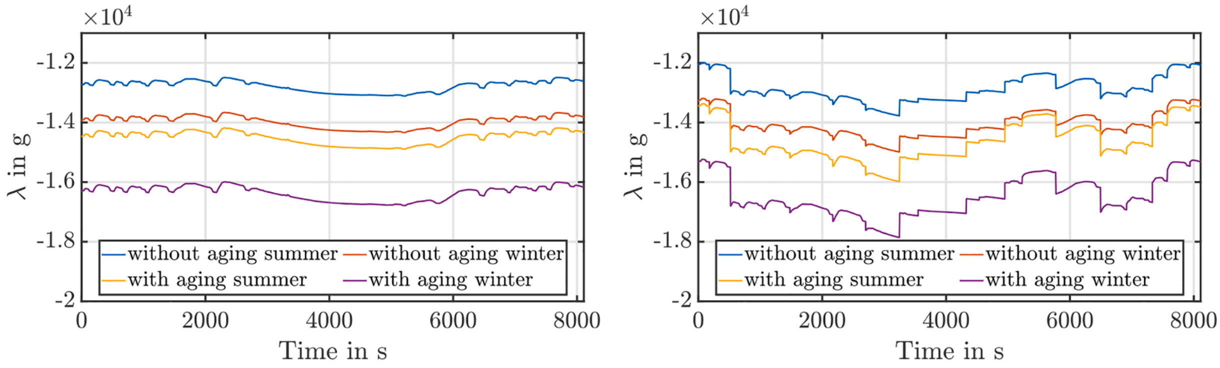

(e) $\lambda(t)$ trajectory from PMP results.

(f) $\lambda(t)$ trajectory from APMP results.

Fig. 16. Performance of energy management strategy with and without fuel cell aging regarding PMP and APMP-based strategy.

Table 4
Fuel economy analysis considering fuel cell aging.

Season	Summer		Winter	
	HD7	*HD7Aging*	*HD7*	*HD7Aging*
$\bar{\lambda}$ (g) of APMP	−12866	−14631	−14073	−16494
$\bar{\lambda}$ (g) of PMP	−12776	−14509	−13976	−16361
Ref.$\lvert\bar{\lambda}\rvert$ from PMP	+0.70%	+0.84%	+0.69%	+0.82%
$\mathbf{m_{H_2}}$ (g) of PMP	32268	33888	42334	42786
$\mathbf{m_{H_2}}$ (g/km) of PMP	221.29	232.40	290.32	293.42
$\mathbf{m_{H_2}}$ (g) of APMP	32680	34386	45502	46060
$\mathbf{m_{H_2}}$ (g/km) of APMP	224.11	235.81	312.04	315.87
$\mathbf{SoC_{end}}$	0.52	0.52	0.52	0.52
Ref.$\mathbf{m_{H_2}}$ from PMP	+1.28%	+1.47%	+1.07%	+1.23%

estimated costate amplitude difference is obvious when various specific curves are used for the APMP strategy, as shown in Fig. 18(f). Then, to evaluate the APMP strategy's robustness against inaccurate fuel cell modeling, the PMP strategy, which uses the specific consumption curve of *HD8*, is used to determine the minimal hydrogen consumption. Thereby, the load power trajectories and the SoC initial and end values resulted from the APMP strategies, with different specific consumption curves used, are inputs for the PMP algorithm. The fuel cell power, SoC, and costate trajectories resulted from the PMP strategy in sub-Fig. 18(a), (c) and (e) are almost the same because the input of the load power trajectories and the SoC boundaries values from the APMP simulations are close.

The deviations in the costate average value under the APMP for *HD7* and *HD7Aging* from the value resulted from the PMP strategy, are shown in Table 6. The fuel economy under inaccurate modeling of the fuel cell system is analyzed in Table 7. The same SoC end value of 0.52 results for APMP under different fuel cell models. The hydrogen consumption

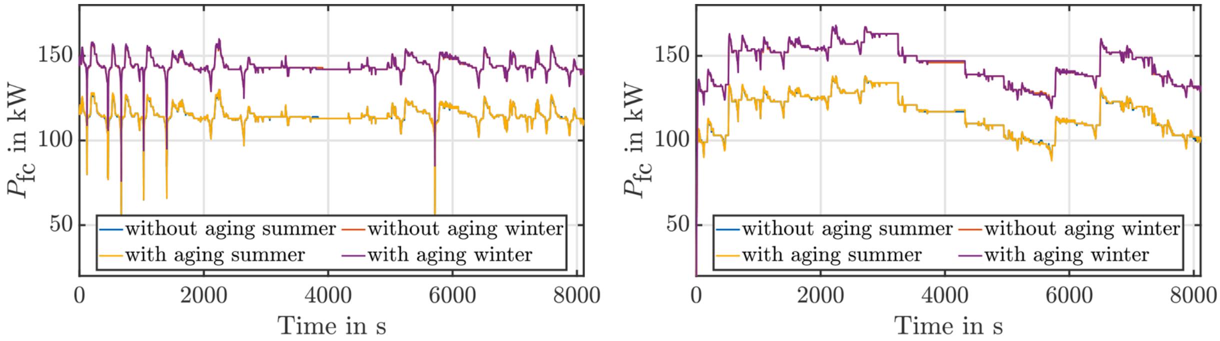

(a) $P_{\mathrm{fc}}(t)$ trajectory from PMP results.

(b) $P_{\mathrm{fc}}(t)$ trajectory from APMP results.

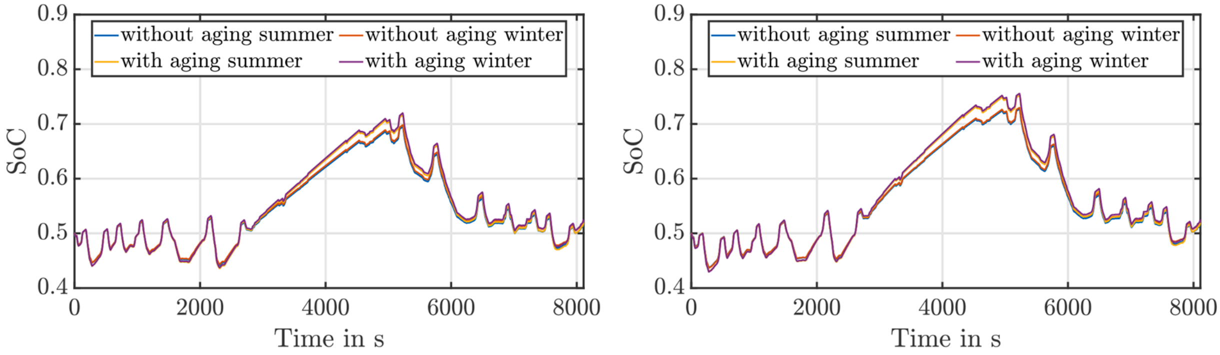

(c) $SoC(t)$ trajectory from PMP results.

(d) $SoC(t)$ trajectory from APMP results.

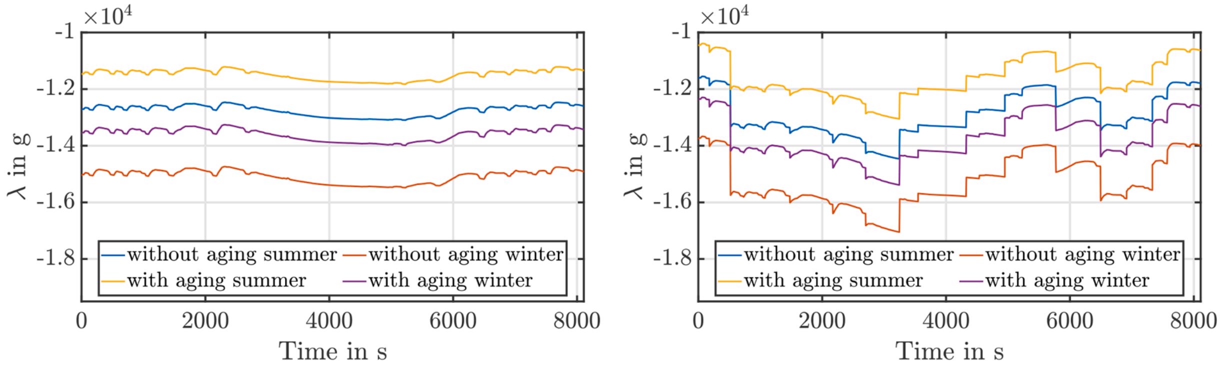

(e) $\lambda(t)$ trajectory from PMP results.

(f) $\lambda(t)$ trajectory from APMP results.

Fig. 17. Performance of energy management strategy with battery aging considered regarding PMP and APMP-based strategy.

Table 5
Fuel economy analysis considering battery aging.

Season	Summer		Winter	
	Origin	Aging	Origin	Aging
$\bar{\lambda}$ (g) of APMP	−12910	−11636	−15257	−13749
$\bar{\lambda}$ (g) of PMP	−12756	−11494	−15084	−13593
Ref.$\lvert\bar{\lambda}\rvert$ from PMP	+1.21%	+1.24%	+1.15%	+1.15%
$\mathbf{m_{H_2}}$ (g) of PMP	31094	31116	41550	41576
$\mathbf{m_{H_2}}$ (g/km) of PMP	213.24	213.39	284.94	285.12
$\mathbf{m_{H_2}}$ (g) of APMP	31554	31584	42102	42140
$\mathbf{m_{H_2}}$ (g/km) of APMP	216.39	216.60	288.73	288.99
$\mathbf{SoC_{end}}$	0.52	0.52	0.52	0.53
Ref.$\mathbf{m_{H_2}}$ from PMP	+1.48%	+1.50%	+1.33%	+1.36%

increase, which uses inaccurate fuel cell models in the APMP strategy, compared to the PMP results, is 1.33% and 1.47% for *HD7* and *HD7Aging* respectively in summer, 1.29%, and 1.31% in winter. Compared to the APMP strategy, which uses the accurate fuel cell model *HD8*, which has more consumption of 1.48% in summer and 1.33% in winter than the corresponding PMP results, the fuel economy's difference is negligible. In conclusion, the excellent fuel economy is maintained, whereby the APMP-based strategy's effectiveness is proved in the case of inaccurate fuel cell modeling, which shows low sensitivity and a high degree of robustness.

4.5. APMP without fuel cell aging accurately known

After a long-term operation, the degradation of the fuel cell increases. It is most likely that the fuel cell's characteristic curves are accurately estimated at the beginning of its lifetime. However, the characteristic curves change after the long-term operation due to

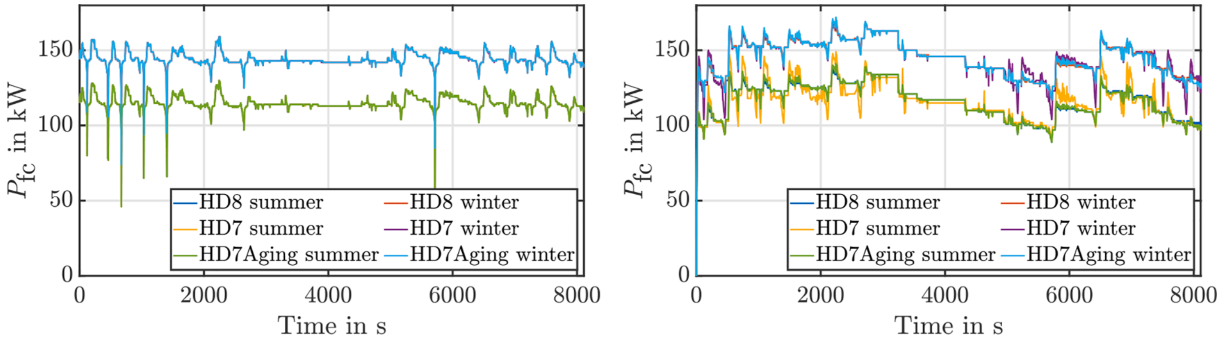

(a) $P_{fc}(t)$ trajectory from PMP results. (b) $P_{fc}(t)$ trajectory from APMP results.

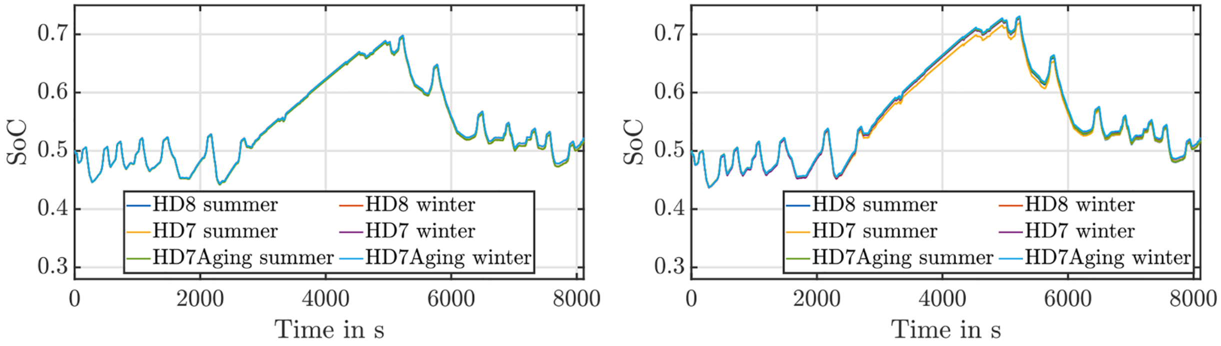

(c) $SoC(t)$ trajectory from PMP results. (d) $SoC(t)$ trajectory from APMP results.

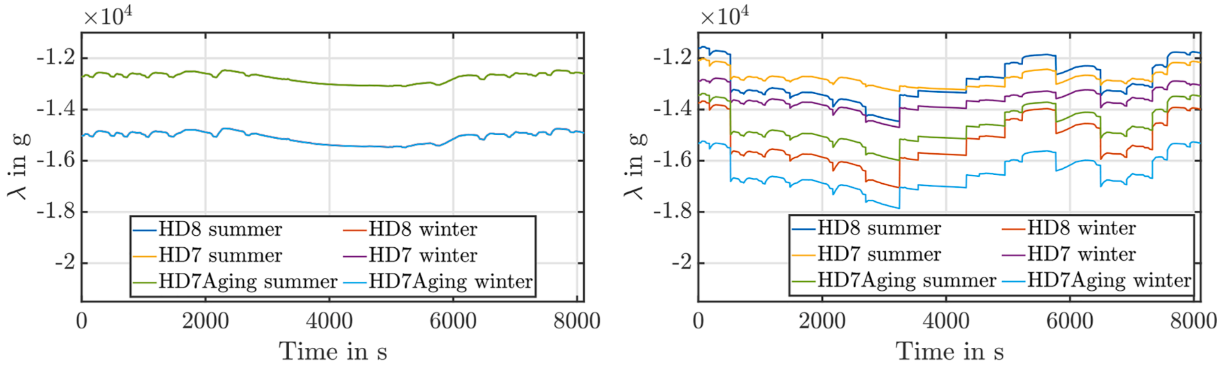

(e) $\lambda(t)$ trajectory from PMP results. (f) $\lambda(t)$ trajectory from APMP results.

Fig. 18. Performance of energy management strategy considering inaccurate estimation of fuel cell systems regarding PMP and APMP-based strategy.

Table 6
Average relative deviations of λ under inaccurate fuel cell modeling.

Season	Summer		Winter	
	HD7	HD7Aging	HD7	HD7Aging
$\bar{\lambda}$ (g) of aging APMP	−12787	−14631	−13628	−16494
Ref.$\lvert\bar{\lambda}\rvert$ from PMP	0.25%	14.7%	9.63%	9.34%

unavoidable degradation, which causes another inconsistency between the actual fuel cell and its model. In this case, energy management maintains using *HD8* as the model of the fuel cell. For the calculation of hydrogen consumption, the fuel cell model *HD8* is used as the original fuel cell without degradation, and the model *HD7* and *HD7Aging* are used as the fuel cell with different degradation degree. The results of PMP with the same degradation degree are considered as the benchmark results for the APMP simulation. Here, the strategy under the driving

Table 7
Fuel economy analysis considering inaccurate estimation of the fuel cell system.

Season	Model in APMP	$\mathbf{m}_{H_2}$ of APMP	$\mathbf{m}_{H_2}$ of PMP	Δm_{H_2}
Summer	HD8	31094 g 213.24 g/km	31554 g 216.39 g/km	+1.48%
	HD7	31092 g 213.22 g/km	31504 g 216.05 g/km	+1.33%
	HD7Aging	31096 g 213.25 g/km	31554 g 216.39 g/km	+1.47%
Winter	HD8	41550 g 284.94 g/km	42102 g 288.73 g/km	+1.33%
	HD7	41540 g 284.87 g/km	42074 g 288.53 g/km	+1.29%
	HD7Aging	41552 g 284.95 g/km	42098 g 288.70 g/km	+1.31%

cycle ENV2 is investigated.

In the APMP simulation, the same fuel cell model *HD8* is used to distribute power. Therefore, the fuel cell power trajectories are the same. For this reason, only PMP results are displayed in Fig. 19, where a low deviation is observed for fuel cell power and SoC trajectories. The λ trajectories drift apart due to the difference between *HD7*, *HD7Aging*, and *HD8*.

The deviation in the costate under the APMP from the costate of the PMP strategy, with the fuel cell model *HD7* and *HD7Aging* separately used for offline calculation, is shown in Table 8. Furthermore, the same SoC end value of 0.52 results from simulations.

The fuel economy due to the undetected deviation of the fuel cell is depicted in Table 9. It is worth mentioning that in calculating hydrogen consumption, the specific consumption curves of the actual fuel cell under different degradation degrees are used and they are *HD8*, *HD7*, and *HD7Aging* sequentially. The slight variation of additional hydrogen consumption in comparison to PMP results is nearly unnoticeable. In conclusion, the excellent fuel economy is maintained, and the effectiveness of the APMP strategy is proved to be not affected by the slight undetected deviation of the fuel cell system.

4.6. APMP under different polynomial approximations for fuel cell consumption modeling

The specific consumption curve is obtained by fitting the experimental data, as shown in Fig. 20(a). Based on the same group of data, different fitting methods can provide a slight difference. Here, eight fuel cell specific consumption curves are fitted, as shown in Fig. 20(b). Among all these models, *HD8*, *HD7*, and *HD8Poly3* are chosen for further detailed analysis as examples. The Fig. 21 shows PMP simulation results of *HD8*, *HD7*, and *HD8Poly3*. The Fig. 22 shows APMP simulation results of *HD8*, *HD7*, and *HD8Poly3*.

Notably, the fuel cell power trajectories nearly overlap for both PMP and APMP results. In comparison to the PMP strategy, the extra hydrogen consumed by the APMP strategy has a slight increment from 1.211% to 1.65%, whereby *HD8* is used to calculate the hydrogen consumption. The values related to fuel efficiency are listed in Table 10. Therefore, the APMP-based strategy is also robust against deviations introduced by curves approximation.

Table 8
Average relative deviations of λ under undetected deviation of fuel cell systems.

Season	Summer		Winter	
	HD7	HD7Aging	HD7	HD7Aging
$\bar{\lambda}$ (g) APMP	−12910	−12910	−15257	−15257
Ref.$\lvert\bar{\lambda}\rvert$ PMP	1.29%	11.02%	13.18%	6.75%

Table 9
Fuel economy analysis considering undetected deviation of fuel cell systems.

Season	Model to calculate $\mathbf{m}_{\mathrm{H}_2}$	$\mathbf{m}_{\mathrm{H}_2}$ of APMP	$\mathbf{m}_{\mathrm{H}_2}$ of PMP	$\Delta \boldsymbol{m}_{\mathrm{H}_2}$
Summer	HD8	31094 g 213.24 g/km	31554 g 216.39 g/km	+1.48%
	HD7	32150 g 220.48 g/km	32596 g 223.54 g/km	+1.39%
	HD7Aging	33886 g 232.38 g/km	34388 g 235.83 g/km	+1.48%
Winter	HD8	41550 g 284.94 g/km	42102 g 288.73 g/km	+1.33%
	HD7	42026 g 288.20 g/km	42486 g 291.35 g/km	+1.09%
	HD7Aging	45502 g 312.04 g/km	46070 g 315.94 g/km	+1.25%

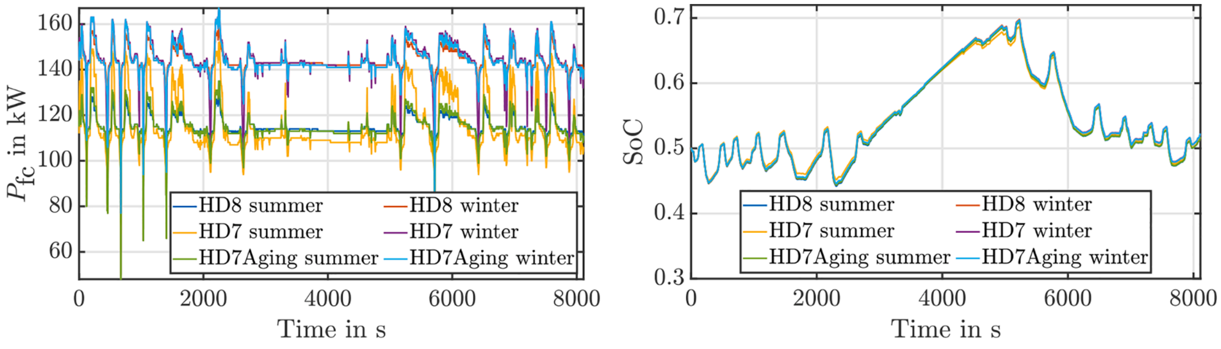

(a) $P_{\mathrm{fc}}(t)$ trajectory. (b) $SoC(t)$ trajectory.

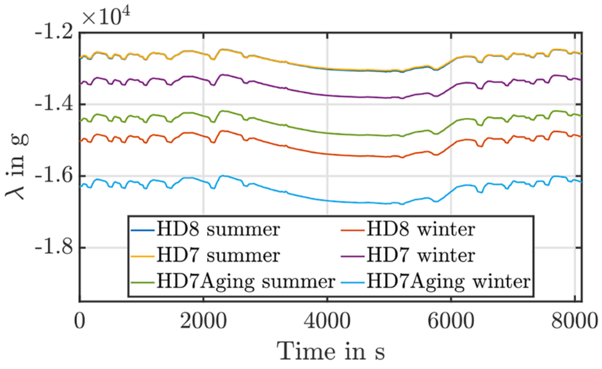

(c) $\lambda(t)$ trajectory.

Fig. 19. Trajectories resulted from the PMP-based strategy under undetected deviation of fuel cell systems.

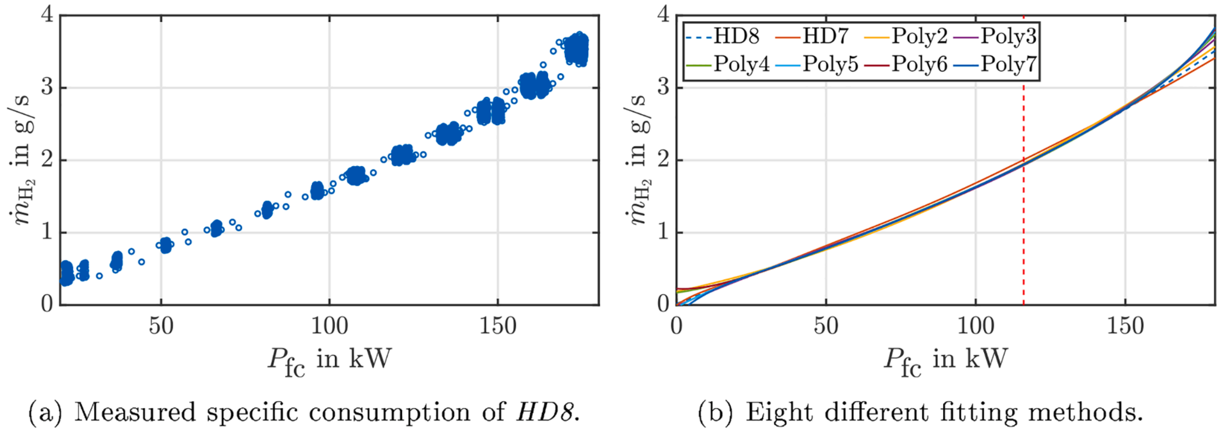

(a) Measured specific consumption of *HD8*. (b) Eight different fitting methods.

Fig. 20. Fitting on the experimental data of the fuel cell system.

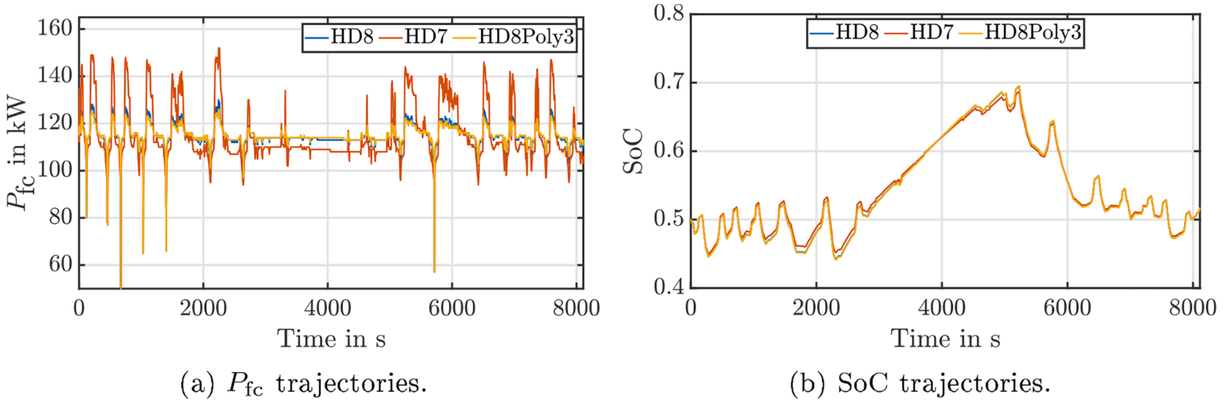

(a) P_{fc} trajectories. (b) SoC trajectories.

Fig. 21. PMP results regarding different fitted fuel cell models.

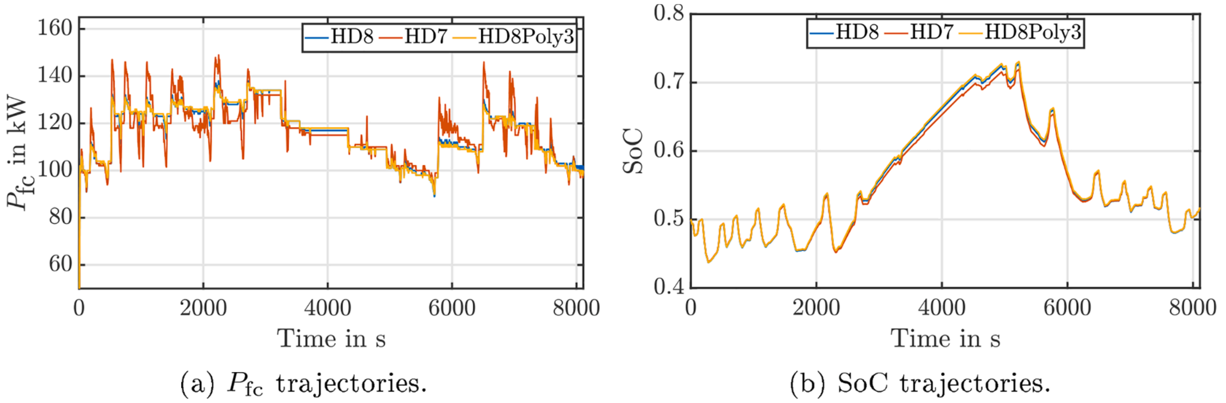

(a) P_{fc} trajectories. (b) SoC trajectories.

Fig. 22. APMP results regarding different fitted fuel cell models.

Table 10
APMP simulation results considering different fitted fuel cell models.

Fitted models	$\mathbf{SoC}_{\mathrm{end}}$	$\mathbf{m}_{\mathrm{H_2}}$ (g/km)	Ref.$\mathbf{m}_{\mathrm{H_2}}$ from PMP
HD7	0.52	223.13	+1.21 %
HD8	0.52	216.39	+1.48 %
HD8Poly3	0.52	215.95	+1.65 %

5. Experimental validation

5.1. *Configuration of test bench*

The configuration, which is utilized in the simulations, is displayed in Fig. 1. However, the configuration of test bench, which is shown in Fig. 23, slightly differs from that of the simulation model. Fig. 24.

The test bench is also powered by two sources, including a fuel cell system and a lithium-ion battery system. The fuel cell system is actively controlled by a unidirectional DC/DC converter, while the lithium-ion battery system is directly connected to the DC bus of the fuel cell output. A bidirectional DC/DC boost converter is applied as an interface

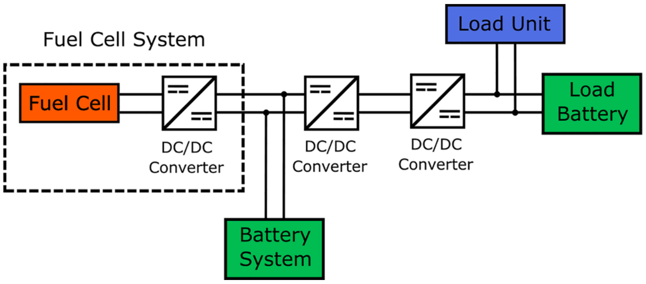

Fig. 23. Schematic of the test bench configuration.

from fuel cell output to the DC-link, which is controlled to maintain the DC-link voltage at 1650 V. Another DC/DC converter is implemented for the load side and controls the load power. Instead of a real driveline consisting of inverters, motors, gears, wheels, and mechanical loads, the load power is emulated by using the load side DC/DC converter. A battery system and a load unit, which transports electrical energy into the network, are used as power sinks. The load battery absorbs high peak power, and the load unit is actively controlled to absorb average fuel cell power.

Due to the technical limitations of the test objects, the system's power is restricted. Thereby, only two of the three branches of the battery system can be used. Therefore, the power demand on the DC-link implemented on the test bench should be downscaled to be about two-thirds of its simulated value. However, the fuel cell system power demand on the test bench should not be downscaled to ensure that energy management strategies' validation regarding fuel economy remains meaningful. Therefore, the load power demanded by the DC link on the test bench is formulated as:

$$P_{\text{load,testbench}}\left(t\right)=\frac{2}{3}\cdot P_{\text{load}}\left(t\right)+\frac{1}{3}\cdot P_{\text{fc}}\left(t\right), \tag{34}$$

whereby $P_{\text{load,testbench}}(t)$ is the implemented load power on the test bench, $P_{\text{load}}(t)$ the simulated load power, and $P_{\text{fc}}(t)$ the simulated fuel cell power. Then, the battery power in the test bench is estimated to be:

$$\begin{aligned} P_{\text{bat,testbench}} &= P_{\text{load,testbench}}(t)-P_{\text{fc}}(t) \\ &= \frac{2}{3}\left(P_{\text{load}}\left(t\right)-P_{\text{fc}}\left(t\right)\right), \end{aligned} \tag{35}$$

Then, the battery power in the test bench is almost two-thirds of the simulated battery power. Because two of the three branches of the battery system are switched on, the measured SoC trajectory after downscaling is close to the results of the initially planned experiments. The comparison of test bench parameters is listed in Table 11.

5.2. *Experimental validation of APMP*

In this section, the effectiveness of the stationary modeling of DC/DC converter, the fuel cell system, and the lithium-ion battery system is validated under driving cycle ENV4.

The modeling of DC/DC converter is validated by comparing the modeled loss power to the measured loss power. The power loss is the difference between the input and output power as follows:

$$P_{\text{loss}}\left(t\right)=P_{\text{fc,meas}}\left(t\right)+P_{\text{bat,meas}}\left(t\right)-P_{\text{dc}-\text{link}}\left(t\right), \tag{36}$$

whereby $P_{\text{fc,meas}}(t)$ is the measured fuel cell power trajectory, $P_{\text{bat,meas}}(t)$ the measured battery power trajectory, and $P_{\text{dc}-\text{link}}(t)$ the measured DC-link power trajectory. The power loss trajectories measured in the test bench and calculated in the model are displayed in Fig. 25. The effectiveness and accuracy of the DC/DC converter modeling is evident as the average measured power loss is 5.42 kW, and that of modeled power loss is 5.84 kW, thus making the average relative difference of 7.75%.

The modeling of the fuel cell system is validated by comparing the model-based calculated hydrogen consumption to the measured one from the test bench, as shown in Fig. 26. The trajectories in Fig. 26(a) nearly overlap, which verifies the effectiveness and accuracy of the fuel cell modeling. The measured final hydrogen consumption is 5687 g, and the modeled final hydrogen consumption is 5626 g. The enlarged view of the trajectories at the end of the driving cycle shows a slight relative difference of 1.07%.

The modeling of the battery system is validated by comparing the simulated battery voltage and SoC to the measured counterparts in the

Table 11
Parameter comparison between the simulation model and test bench.

Parameters	Modeling	Test bench
Maximum fuel cell power	180 kW	150 kW
Minimum fuel cell power	20 kW	20 kW
Maximum charge current per branch	300 A	250 A
Maximum discharge current per branch	−300 A	−250 A
Maximum battery charge power	730 kW	600 kW
Maximum battery discharge power	730 kW	−600 kW
Number of battery branches	3	2
Number of passengers	120	60

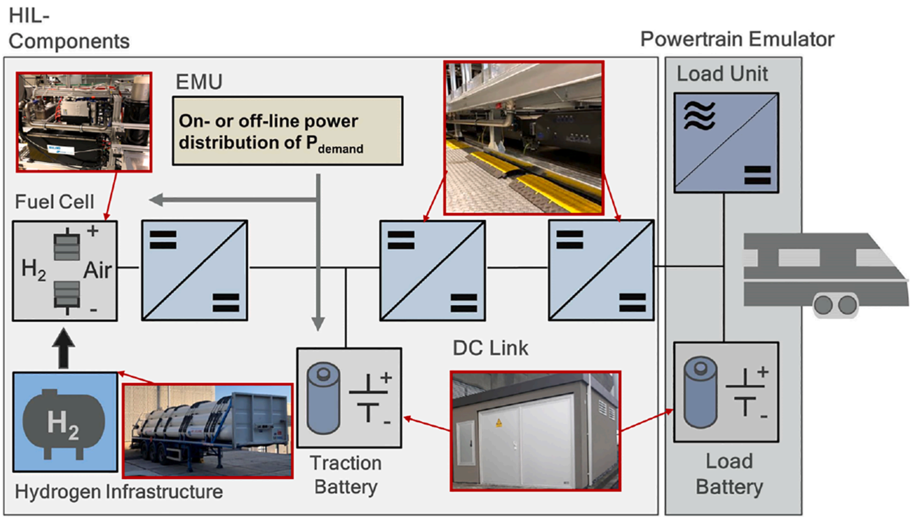

Fig. 24. Configuration of the test bench.

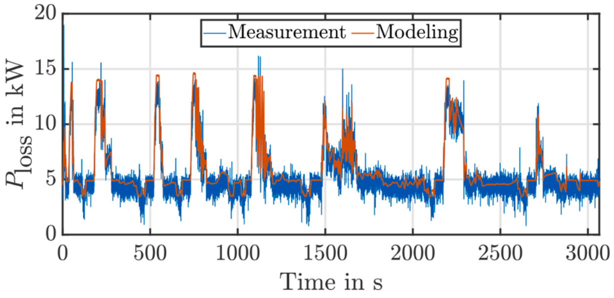

Fig. 25. Validation of DC/DC converter modeling via power loss trajectories.

test bench, respectively, as shown in Fig. 27. Although the discretization procedure of SoC intrinsically provides a deviation of 1% compared to its original value, the measured SoC value is consistent with the simulation result, as shown in Fig. 27(b). The trajectories of measured battery voltage and modeled battery voltage in Fig. 27(a) nearly overlap.

In order to validate the effectiveness of the APMP-based strategy on test bench, the measured results from the test bench are compared to the offline PMP results, which is regarded as the benchmark. The measured power demand at DC-link and SoC end value of 0.5, the same as the initial value, from the test bench are utilized as inputs to the offline PMP calculation. The comparison of results under driving cycle ENV4 is displayed in Fig. 28, whereby *HD8* is utilized as the fuel cell model.

The fuel cell power trajectories of measured results in Fig. 28(a) are mainly matching those of PMP results. The average value and average relative devaition are included in Table 12. An additional hydrogen consumption on test bench of 1.09% compared to PMP, which shows a perfect fuel economy, verifies the effectiveness of APMP-based strategy on the test bench.

5.3. Validation of the Robustness of APMP

In order to validate the effectiveness of the APMP-based strategy under inaccurate estimation of fuel cell characteristic curves, the test bench is operated with EMS utilizing different fuel cell specific consumption curves, i.e., *HD7*, *HD7Aging*, *HD8Poly3*, and *HD8Poly5*, as shown in Fig. 29.

The measured fuel cell power and SoC trajectories from the test bench under the driving cycle ENV4 are displayed in Fig. 30. The measured results compared to the offline PMP results are displayed in Figs. 31 and 32, whereby the inputs to offline PMP calculation are the measured power demand at DC-link and SoC end value from the test bench.

It is evident that the fuel cell power trajectories of measured results in Fig. 31 are mostly around the corresponding PMP results. And the SoC trajectories in Fig. 32 are also approximately consistent with the PMP results. The average value and average relative deviation are included in Table 13, where the fuel economy based on the measurement is also analyzed. The additional hydrogen consumption of the test bench in reference to PMP result is only 1.19 ~2.70%, which slightly deviates from the benchmark of 1.09% under accurate fuel cell modeling by using *HD8*. Therefore, the effectiveness of the APMP-based strategy with inaccurate estimation of fuel cell characteristic curves is verified.

6. Conclusions

In this contribution, an offline PMP strategy, which considers the

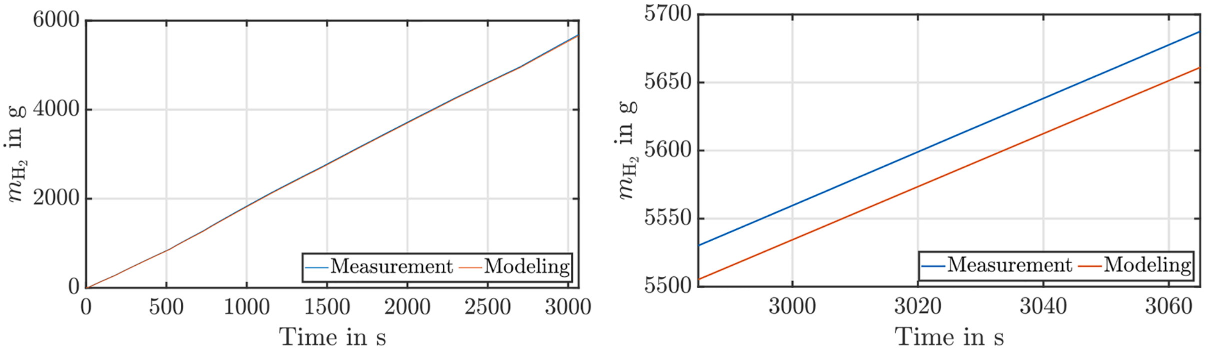

(a) $m_{\mathrm{H}_2}(t)$ without zoom in.

(b) $m_{\mathrm{H}_2}(t)$ with zoom in at the end of the driving cycle.

Fig. 26. Validation of fuel cell modeling via hydrogen consumption trajectories.

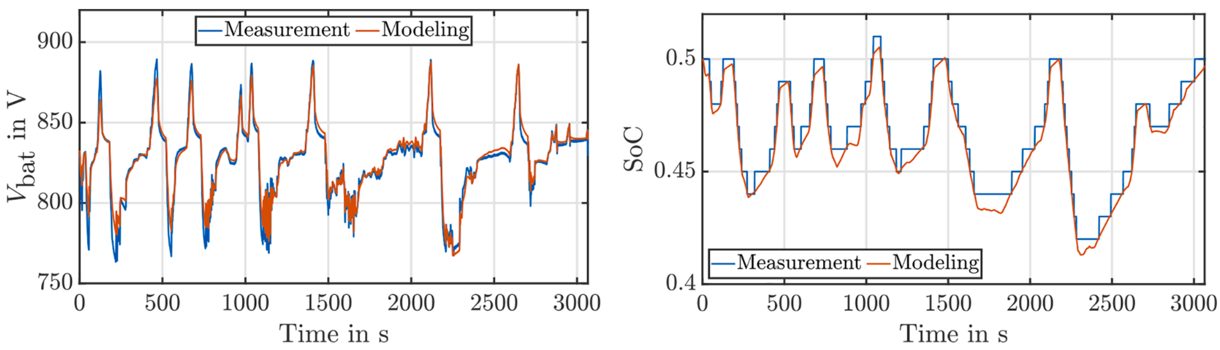

(a) $V_{\text{bat}}(t)$.

(b) $SoC(t)$.

Fig. 27. Validation of battery modeling via battery voltage and SoC trajectories.

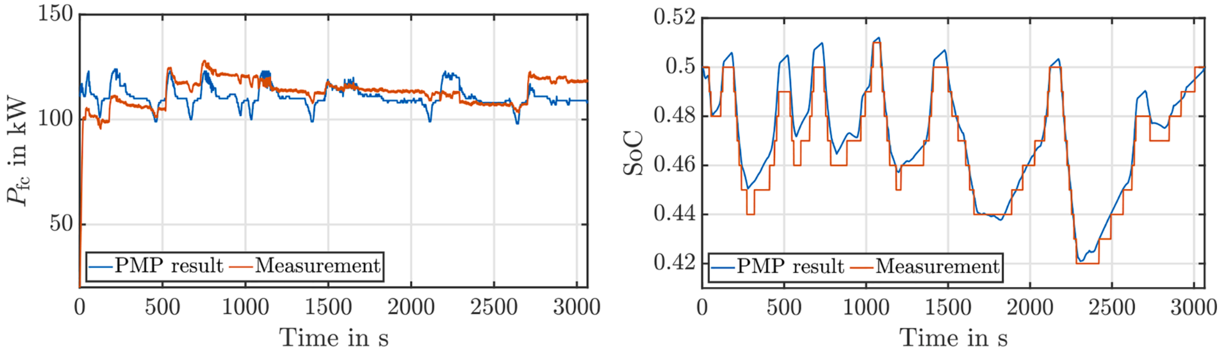

(a) P_{fc}.

(b) SoC.

Fig. 28. Validation of APMP-based strategy in reference to PMP-based strategy.

Table 12
Comparison between test bench measurement of APMP and PMP result.

Data source	$\overline{P}_{fc}$ (kW)	Ref.$\overline{P}_{fc}$ from PMP	m_{H_2} (g/km)	Ref.m_{H_2} from PMP
PMP	110.92	–	160.30	–
Test bench	112.89	1.78%	162.05	1.09%

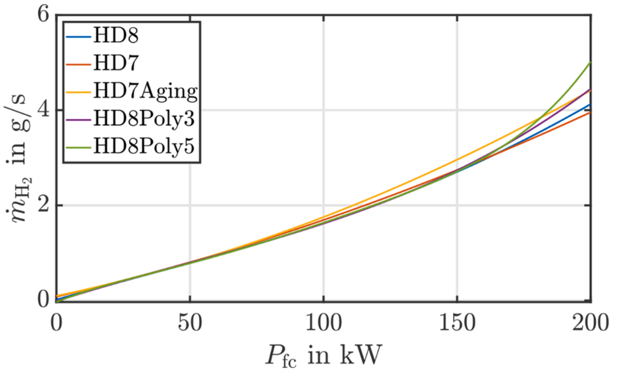

Fig. 29. Different fuel cell specific consumption curves utilized in test bench.

relaxation process due to the resistance-capacitor branches in batteries, is implemented to provide accurate reference results for evaluating online strategies. After that, the most significant challenge faced with the APMP or ECMS-based strategy of adaptively estimating the costate is solved by an analytical formula based on the energy conservation principle. The robustness of the model-based APMP strategy regarding the fuel economy against various uncertainties and aging effects are validated through simulation and measurement on the test bench. Under various aging and uncertainty conditions, a maximum of 1.5% more hydrogen consumption is obtained in the simulation results compared to offline PMP results. In the test bench measurement results under various uncertain conditions, hydrogen consumption is at most 2.7% higher than the optimal offline strategy. Due to its model-based characteristic, this strategy is universal, scalable, robust, and adaptive, which can be used not only for hybrid trains but also for other transportation and stationary applications.

CRediT authorship contribution statement

Hujun Peng: Conceptualization, Methodology, Formal analysis, Investigation, Validation, Writing - Original Draft. **Hanqing Cao:** Software, Data Curation, Validation, Writing - Original Draft. **Steffen Dirkes:** Investigation, Writing - Review & Editing, Resources. **Zhu Chen:** Data Curation, Software, Visualization. **Kai Deng:** Investigation, Writing - Review & Editing. **Jonas Gottschalk:** Investigation. **Cem Ünlübayir:** Writing - Review & Editing, Investigation. **Andreas Thul:** Project Administration, Writing - Review & Editing. **Lars Löwenstein:** Resources, Writing - Review & Editing. **Dirk Uwe Sauer:** Writing - Review & Editing, Funding acquisition. **Stefan Pischinger:** Funding acquisition, Resources. **Kay Hameyer:** Supervisor, Funding acquisition, Writing- Reviewing and Editing.

Declaration of Competing Interest

The authors declare that they have no known competing financial interests or personal relationships that could have appeared to influence the work reported in this paper.

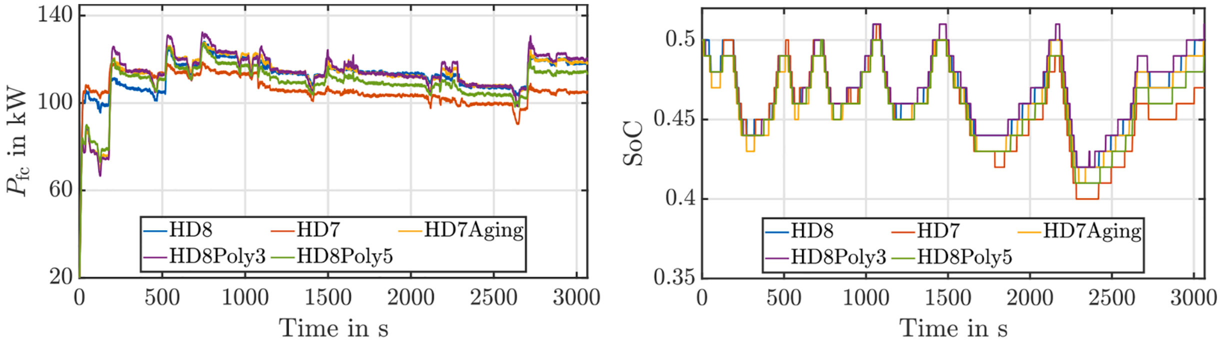

(a) P_{fc}.

(b) SoC.

Fig. 30. Measured results of APMP-based strategy with inaccurate estimation of fuel cell.

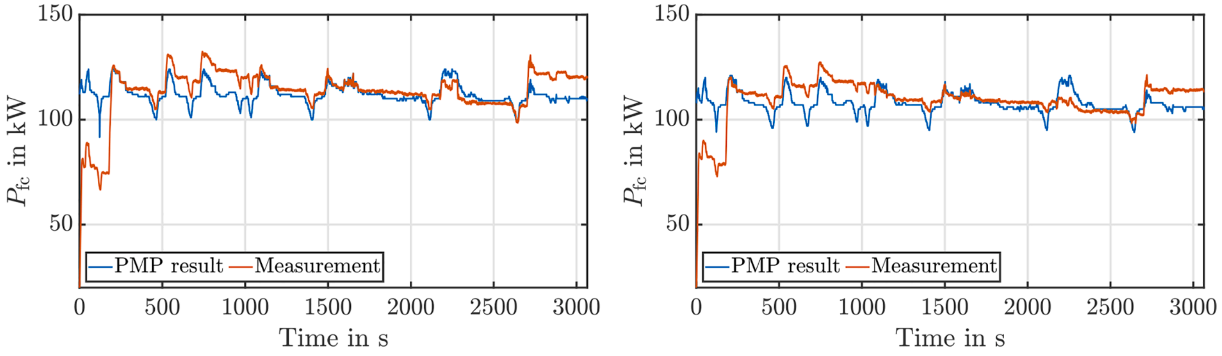

(a) HD7.

(b) HD7Aging.

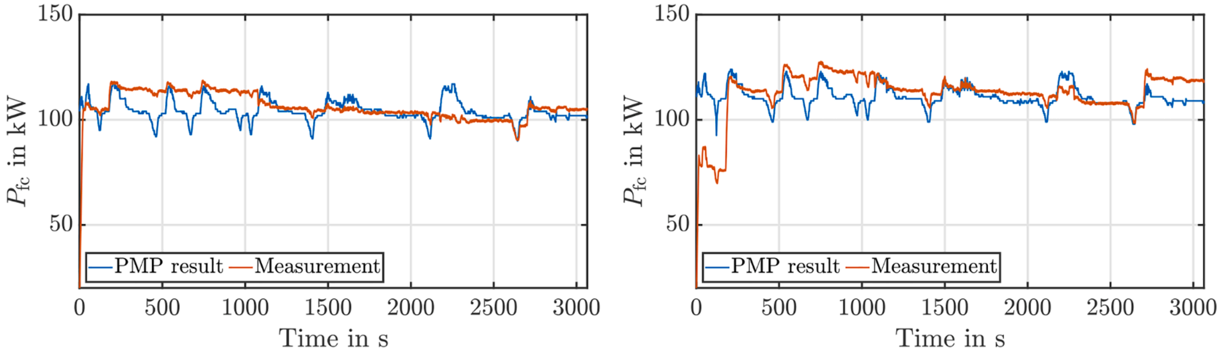

(c) HD8Poly3.

(d) HD8Poly5.

Fig. 31. P_{fc} trajectories from the APMP-based strategy under inaccurate estimation of fuel cell in reference to the PMP-based strategy.

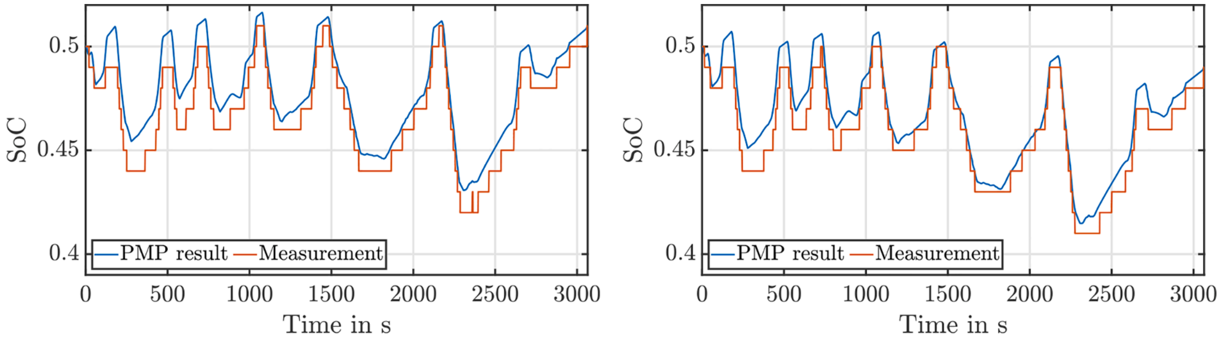

(a) HD7.

(b) HD7Aging.

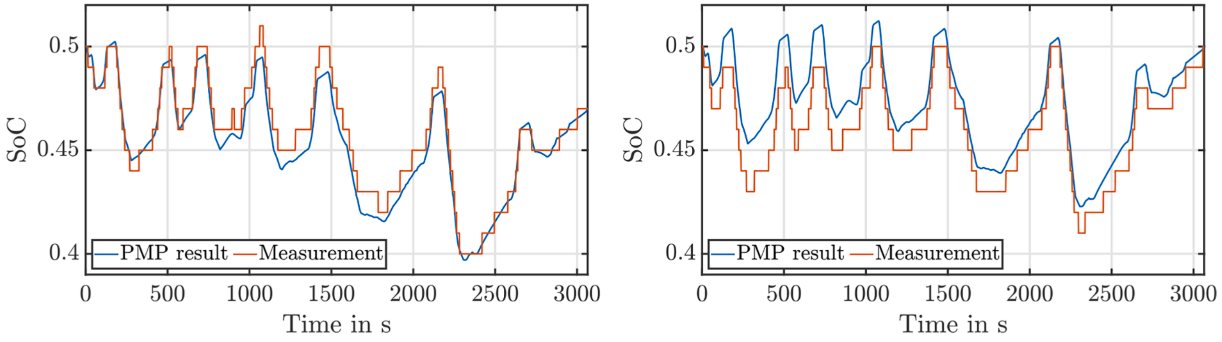

(c) HD8Poly3.

(d) HD8Poly5.

Fig. 32. *SoC*trajectories from the APMP-based strategy under inaccurate estimation of fuel cell in reference to the PMP-based strategy.

Table 13
Validation of APMP based on test bench measurement, compared to PMP results, where T.B. represents test bench.

Model	Data source	$\overline{P}_{fc}$ (kW)	Ref.$\overline{P}_{fc}$ PMP	SoC end	m_{H_2} (g/km)	Ref. PMP
HD7	PMP	112.09	–	0.51	162.32	–
	T.B.	113.41	1.18%	0.51	164.25	1.19%
HD7	PMP	107.88	–	0.49	155.05	–
Aging	T.B.	109.32	1.33%	0.49	156.94	1.22%
HD8	PMP	104.25	–	0.47	148.96	–
Poly3	T.B.	106.31	1.98%	0.47	152.01	2.05%
HD8	PMP	110.87	–	0.50	160.21	–
Poly5	T.B.	112.78	1.72%	0.50	164.53	2.70%

References

[1] Communication from the commission to the european parliament, the council, the european economic and social committee and the committee of the regions, https://ec.europa.eu/energy/sites/ener/files/hydrogen_strategy.pdf, accessed July 4, 2020.

[2] Alstom’s hydrogen train coradia ilint completes successful tests in the netherlands, https://www.alstom.com/press-releases-news/2020/3/alstoms-hydrogen-train-coradia-ilint-completes-successful-tests, accessed July 4, 2020.

[3] Development and validation of a high-power-fuel-cell-drive-train for hybrid-emu-railways, https://www.isea.rwth-aachen.de/cms/ISEA/Forschung/Projekte/Oeffentliche-Projekte/Laufende-Projekte/ qate/X-EMU/?lidx=1, accessed July 4, 2020.

[4] Wang Y, Moura SJ, Advani SG, Prasad AK. Power management system for a fuel cell/battery hybrid vehicle incorporating fuel cell and battery degradation. Int J Hydrogen Energy 2019;44(16):8479–92.

[5] Ahmadi S, Bathaee S, Hosseinpour AH. Improving fuel economy and performance of a fuel-cell hybrid electric vehicle (fuel-cell, battery, and ultra-capacitor) using optimized energy management strategy. Energy Conv Manage 2018;160:74–84.

[6] Fu Z, Zhu L, Tao F, Si P, Sun L. Optimization based energy management strategy for fuel cell/battery/ultracapacitor hybrid vehicle considering fuel economy and fuel cell lifespan. Int J Hydrogen Energy 2020;45(15):8875–86.

[7] Wu Y, Tan H, Peng J, Zhang H, He H. Deep reinforcement learning of energy management with continuous control strategy and traffic information for a series-parallel plug-in hybrid electric bus. Appl Energy 2019;247:454–66.

[8] Xu B, Rathod D, Zhang D, Yebi A, Zhang X, Li X, Filipi Z. Parametric study on reinforcement learning optimized energy management strategy for a hybrid electric vehicle. Appl Energy 2020;259. 114200.

[9] Peng H, Li J, Deng K, Thul A, Li W, Löwenstein L, Sauer DU, Hameyer K. An efficient optimum energy management strategy using parallel dynamic programming for a hybrid train powered by fuel-cells and batteries. In: 2019 IEEE Vehicle Power and Propulsion Conference (VPPC); 2019. p. 1–7.

[10] Peng H, Li J, Löwenstein L, Hameyer K. A scalable, causal, adaptive energy management strategy based on optimal control theory for a fuel cell hybrid railway vehicle. Appl Energy 2020;267. 114987.

[11] Peng H, Li J, Thul A, Deng K, Ünlübayir C, Löwenstein L, Hameyer K. A scalable, causal, adaptive rule-based energy management for fuel cell hybrid railway vehicles learned from results of dynamic programming. eTransportation 2020: 100057.

[12] Yan Y, Li Q, Chen W, Su B, Liu J, Ma L. Optimal energy management and control in multimode equivalent energy consumption of fuel cell/supercapacitor of hybrid electric tram. IEEE Trans Ind Electr 2019;66(8):6065–76. https://doi.org/10.1109/TIE.2018.2871792.

[13] Li X, Wang Y, Yang D, Chen Z. Adaptive energy management strategy for fuel cell/battery hybrid vehicles using pontryagin’s minimal principle. J Power Sour 2019; 440. 227105.

[14] Tian X, Cai Y, Sun X, Zhu Z, Xu Y. An adaptive ecms with driving style recognition for energy optimization of parallel hybrid electric buses. Energy 2019;189. 116151.

[15] Rezaei A, Burl JB, Zhou B. Estimation of the ecms equivalent factor bounds for hybrid electric vehicles. IEEE Trans Control Syst Technol 2018;26(6):2198–205.

[16] Rezaei A, Burl JB, Zhou B, Rezaei M. A new real-time optimal energy management strategy for parallel hybrid electric vehicles. IEEE Trans Control Syst Technol 2019; 27(2):830–7.

[17] Peng F, Zhao Y, Chen T, Zhang X, Chen W, Zhou D, Li Q. Development of robust suboptimal real-time power sharing strategy for modern fuel cell based hybrid tramways considering operational uncertainties and performance degradation. Appl Energy 2018;226:503–21.

[18] Schmittinger W, Vahidi A. A review of the main parameters influencing long-term performance and durability of pem fuel cells. J Power Sour 2008;180(1):1–14. https://doi.org/10.1016/j.jpowsour.2008.01.070.

[19] Li H, Ravey A, N’Diaye A, Djerdir A. Online adaptive equivalent consumption minimization strategy for fuel cell hybrid electric vehicle considering power sources degradation. Energy Conv Manage 2019;192:133–49.